

How to measure galaxy-galaxy-galaxy-lensing with higher precision and accuracy

Laila Linke¹, Patrick Simon¹, Peter Schneider¹, and Stefan Hilbert^{2,3}

¹ Argelander-Institut für Astronomie, Universität Bonn, Auf dem Hügel 71, 53121 Bonn, Germany
e-mail: llinke@astro.uni-bonn.de

² Exzellenzcluster Universe, Boltzmannstr. 2, 85748 Garching, Germany

³ Ludwig-Maximilians-Universität, Universitäts-Sternwarte, Scheinerstr.1, 81679 München, Germany

Received XXX; accepted YYY

ABSTRACT

Context. Galaxy-galaxy-galaxy lensing (G3L) is a powerful tool for constraining the three-point correlation between the galaxy and the matter field and thereby models of galaxy evolution.

Aims. We propose three improvements to current measurements of G3L, designed to improve the precision and the accuracy by using the galaxies' redshifts and removing biases of the estimator. We further show how to account for lens galaxy magnification by the cosmic large-scale structure and how to convert the G3L signal from angular to physical scales.

Methods. The improvements are tested on simple mock data and simulated data based on the Millennium Run with an implemented semi-analytic model of galaxies.

Results. Our improvements increase the signal-to-noise ratio by on average 35 % at angular scales between 0.1 and 10' and physical scales between 0.02 and 2 h^{-1} Mpc. They also remove the bias of the G3L estimator at angular scales below 1', which was originally up to 40 %. The signal due to lens magnification is approximately 10 % of the total signal.

Key words. Gravitational lensing: weak – cosmology: observations – large-scale structure – Galaxies: evolution

1. Introduction

In the current standard model of cosmology the majority of matter in the Universe is dark and only interacts gravitationally (Planck Collaboration et al. 2016; Hildebrandt et al. 2017). While the formation of dark-matter halos and the cosmic large-scale structure has been successfully modelled by N -body simulations (see e.g. Springel et al. 2005), the interplay between dark and baryonic matter is still not well understood. Observational tools are needed to discriminate between various semi-analytic models of galaxy evolution (SAMs; see e.g. Henriques et al. 2015; Lacey et al. 2016) and to test the predictions of hydrodynamical simulations (see e.g. Crain et al. 2015; Vogelsberger et al. 2014).

One promising tool is galaxy-galaxy-galaxy-lensing (G3L), first proposed by Schneider & Watts (2005). It involves measuring the three-point correlation function between the galaxy and matter distribution, by either evaluating the gravitational lensing shear of background galaxies around foreground galaxy pairs (lens-lens-shear correlation) or the lensing shear of background galaxy pairs around single foreground galaxies (lens-shear-shear correlation).

The three-point correlation between pairs of lens galaxies and the shear has been used to detect inter-cluster filaments, by stacking the lensing shear around galaxy pairs separated by several Mpc (Mead et al. 2010; Clampitt et al. 2016). In this work, though, we concentrate on the lens-lens-shear correlation function at smaller scales of hundreds of kpc, to measure the correlation between the mass distribution and galaxy pairs which lie mostly in the same halo. This function was measured successfully in the Red Cluster Sequence Survey by Simon et al. (2008)

and the Canada-France-Hawaii-Lensing Survey (CFHTLenS) by Simon et al. (2013). Furthermore, as shown by Saghiiha et al. (2017), it can better distinguish between models of galaxy evolution than galaxy-galaxy lensing (GGL), where the shear of single source galaxies around single lens galaxies is measured (see e.g. Mandelbaum et al. 2006). Nonetheless, the signal of G3L is lower than that of GGL by an order of magnitude, so improving the signal-to-noise ratio (SNR) is important for the observation and interpretation of G3L.

As of now, G3L measurements have been undertaken only with galaxy catalogues from photometric surveys without precise redshift estimates. Consequently, pairs of lens galaxies which are physically close and therefore highly correlated were treated with the same weight as galaxy pairs separated along the line of sight which have little to no correlation. These separated galaxies decrease the signal and lower the SNR (Simon et al. 2019).

Additionally, G3L is impacted by the magnification of lens galaxies due to the cosmic large-scale structure (LSS) in front of the lenses (Bartelmann & Schneider 2001). This magnification affects the selection function and thereby the number density of lens galaxies in a survey. As source galaxies are also lensed by the LSS, the shear of sources is correlated with the lens magnification and an additional correlation signal arises. This signal has not yet been quantified for G3L, but was found to impact GGL by up to 5 % in CFHTLenS (Simon & Hilbert 2018).

Here, we introduce three improvements to the G3L estimator used by Simon et al. (2008, 2013): (i) weighting the lens galaxy pairs according to their redshift difference, (ii) using a new binning method for the correlation function to reduce biases, and (iii) estimating the magnification bias with lens galaxies sepa-

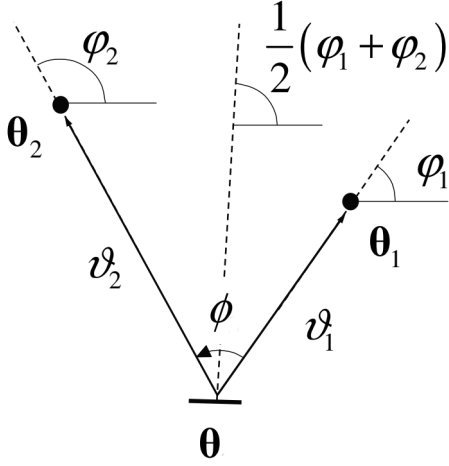


Fig. 1: Geometry of a G3L configuration with one source and two lens galaxies. Adapted from [Schneider & Watts \(2005\)](#).

rated along the line-of-sight. We also show how to measure the correlation in terms of physical instead of angular separation and weigh the signal by the critical surface mass density Σ_{crit} , as is common for GGL (e.g. [Mandelbaum et al. 2006](#)). Thereby, the signal no longer depends on the redshift distribution of source galaxies. To test the impact of our improvements, we apply the new estimator to simple mock data, for which we can directly calculate the expected aperture statistics, and to simulated data based on the Millennium Run ([Springel et al. 2005](#); MR) with the SAM by [Henriques et al. \(2015; H15\)](#).

This paper is structured as follows: Section 2 defines the fundamental quantities of G3L, and gives the estimator for the three-point correlation function by [Simon et al. \(2008\)](#). Section 3 explains our new estimator with redshift weighting and the new binning scheme, as well as how to convert the estimator to physical units and estimate the effect of lens magnification. We describe our simulated data set from the MR in Sect. 4. The results of applying our improved measurement scheme to the data are given in Sect. 5 and discussed in Sect. 6

2. Fundamentals of galaxy-galaxy-galaxy-lensing

G3L is a weak gravitational lensing effect, first discussed by [Schneider & Watts \(2005\)](#); for a review on weak lensing, see [Bartelmann & Schneider 2001](#)). In this work we concentrate on systems of two lens and one source galaxy, whose geometric configuration projected onto the sky is shown in Fig. 1. The main observable of G3L in these systems is the three-point correlation function $\tilde{\mathcal{G}}$ of the projected lens galaxy number density $N(\boldsymbol{\theta})$ and tangential gravitational lensing shear γ_t , given by

$$\tilde{\mathcal{G}}(\boldsymbol{\vartheta}_1, \boldsymbol{\vartheta}_2) = \frac{1}{N^2} \langle N(\boldsymbol{\theta} + \boldsymbol{\vartheta}_1) N(\boldsymbol{\theta} + \boldsymbol{\vartheta}_2) \gamma_t(\boldsymbol{\theta}) \rangle. \quad (1)$$

The tangential shear is measured with respect to the bisector of the angle ϕ between the lens positions $\boldsymbol{\theta} + \boldsymbol{\vartheta}_1$ and $\boldsymbol{\theta} + \boldsymbol{\vartheta}_2$. Due to the isotropy and homogeneity of the matter density field, $\tilde{\mathcal{G}}$ only depends on the lens-source-separations ϑ_1 and ϑ_2 and the opening angle ϕ , so we write

$$\tilde{\mathcal{G}}(\boldsymbol{\vartheta}_1, \boldsymbol{\vartheta}_2) \equiv \tilde{\mathcal{G}}(\vartheta_1, \vartheta_2, \phi). \quad (2)$$

We can estimate $\tilde{\mathcal{G}}(\vartheta_1, \vartheta_2, \phi)$ by averaging the tangential ellipticities of all lens-lens-source triplets where $\boldsymbol{\vartheta}_1$ ($\boldsymbol{\vartheta}_2$) is the separation between the first (second) lens and the source. As discussed by [Simon et al. \(2008\)](#), this average is an estimator of

$$\frac{\langle N(\boldsymbol{\theta} + \boldsymbol{\vartheta}_1) N(\boldsymbol{\theta} + \boldsymbol{\vartheta}_2) \gamma_t(\boldsymbol{\theta}) \rangle}{\langle N(\boldsymbol{\theta} + \boldsymbol{\vartheta}_1) N(\boldsymbol{\theta} + \boldsymbol{\vartheta}_2) \rangle} = \frac{\tilde{\mathcal{G}}(\vartheta_1, \vartheta_2, \phi)}{1 + \omega(|\boldsymbol{\vartheta}_1 - \boldsymbol{\vartheta}_2|)}, \quad (3)$$

with the angular two-point correlation function ω of lens galaxies. Using the complex ellipticity ϵ_k of source galaxies as estimator of their complex lensing shears, Eq. (3) implies that $\tilde{\mathcal{G}}$ can be estimated for each bin b of ϑ_1 , ϑ_2 and ϕ by a triple sum over all N_d lenses and N_s sources by

$$\tilde{\mathcal{G}}_{\text{est}}(b) = - \frac{\sum_{i,j=1}^{N_d} \sum_{k=1}^{N_s} w_k \epsilon_k e^{-i(\varphi_{ik} + \varphi_{jk})} [1 + \omega(|\boldsymbol{\theta}_i - \boldsymbol{\theta}_j|)] \Delta_{ijk}(b)}{\sum_{i,j=1}^{N_d} \sum_{k=1}^{N_s} w_k \Delta_{ijk}(b)} \quad (4)$$

$$=: - \frac{\sum_{ijk} w_k \epsilon_k e^{-i(\varphi_{ik} + \varphi_{jk})} [1 + \omega(|\boldsymbol{\theta}_i - \boldsymbol{\theta}_j|)] \Delta_{ijk}(b)}{\sum_{ijk} w_k \Delta_{ijk}(b)}, \quad (5)$$

with

$$\Delta_{ijk}(b) = \begin{cases} 1 & \text{for } (|\boldsymbol{\theta}_i - \boldsymbol{\theta}_k|, |\boldsymbol{\theta}_k - \boldsymbol{\theta}_j|, \phi_{ijk}) \in b \\ 0 & \text{otherwise} \end{cases}. \quad (6)$$

The angle φ_{ik} (φ_{jk}) is the polar angle of the lens-source separation vector $\boldsymbol{\theta}_i - \boldsymbol{\theta}_k$ ($\boldsymbol{\theta}_j - \boldsymbol{\theta}_k$) and ϕ_{ijk} is the opening angle between $\boldsymbol{\theta}_i - \boldsymbol{\theta}_k$ and $\boldsymbol{\theta}_j - \boldsymbol{\theta}_k$ (see Fig. 1; $\boldsymbol{\theta}_i - \boldsymbol{\theta}_k$ and $\boldsymbol{\theta}_j - \boldsymbol{\theta}_k$ correspond to $\boldsymbol{\vartheta}_1$ and $\boldsymbol{\vartheta}_2$, ϕ_{ijk} corresponds to ϕ). The w_k are weights of the measured ellipticities. For the application of the estimator to observational data, a higher weight should be assigned to sources with more precise shape measurements, while sources with less precise shapes should be down weighted. As we apply the estimator to simulated data, we set $w_k \equiv 1$ throughout this work. The phase factor and minus sign in Eq. (4) are due to the definition of tangential and cross shear in terms of the Cartesian shear components.

In order to estimate ω , we use ‘‘randoms’’. These are mock galaxies, which are distributed unclustered on the sky, but which obey the same selection function as the lens galaxies. With these randoms, we estimate ω with the Landy–Szalay estimator ([Landy & Szalay 1993](#))

$$\omega(\theta) = \frac{N_r^2 DD(\theta)}{N_d^2 RR(\theta)} - 2 \frac{N_r DR(\theta)}{N_d RR(\theta)} + 1. \quad (7)$$

Here, $DD(\theta)$ is the paircount of the N_d lens galaxies, $RR(\theta)$ is the paircount of the N_r randoms and $DR(\theta)$ is the cross paircount of lenses and randoms at separation θ .

Since the correlation function $\tilde{\mathcal{G}}$ contains both the effect of G3L and GGL, we convert it to aperture statistics that only include the G3L signal. Aperture statistics are expectation values of products of the aperture number count \mathcal{N}_θ and the aperture mass $M_{\text{ap},\theta}$. These are defined as ([Bartelmann & Schneider 2001](#))

$$\mathcal{N}_\theta(\boldsymbol{\vartheta}) = \frac{1}{N} \int d^2\boldsymbol{\vartheta}' U_\theta(|\boldsymbol{\vartheta} - \boldsymbol{\vartheta}'|) N(\boldsymbol{\vartheta}'), \quad (8)$$

and

$$M_{\text{ap},\theta}(\boldsymbol{\vartheta}) = \int d^2\boldsymbol{\vartheta}' U_\theta(|\boldsymbol{\vartheta} - \boldsymbol{\vartheta}'|) \kappa(\boldsymbol{\vartheta}'), \quad (9)$$

with the projected galaxy number density $N(\boldsymbol{\vartheta})$, the lensing convergence $\kappa(\boldsymbol{\vartheta})$, and the filter function $U_\theta(\boldsymbol{\vartheta})$ with characteristic scale θ . This filter function needs to be compensated, that is $\int_0^\infty d\vartheta \vartheta U_\theta(\boldsymbol{\vartheta}) = 0$. For each U_θ , an associated filter function Q_θ can be defined by

$$Q_\theta(\boldsymbol{\vartheta}) = \frac{2}{\vartheta^2} \int_0^\vartheta d\vartheta' \vartheta' U_\theta(\boldsymbol{\vartheta}') - U_\theta(\boldsymbol{\vartheta}). \quad (10)$$

With this filter Q_θ ,

$$M_{\text{ap},\theta}(\boldsymbol{\vartheta}) + i M_{\perp,\theta}(\boldsymbol{\vartheta}) = \int d^2\vartheta' Q_\theta(|\boldsymbol{\vartheta} - \boldsymbol{\vartheta}'|) [\gamma_t(\boldsymbol{\vartheta}') + i \gamma_\times(\boldsymbol{\vartheta}')], \quad (11)$$

where $M_{\perp,\theta}$ is the B-mode of the aperture mass.

With the lens-lens-shear correlation function, we study the aperture statistics $\langle \mathcal{N}^2 M_{\text{ap}} \rangle$ and $\langle \mathcal{N}^2 M_{\perp} \rangle$, given by

$$\begin{aligned} & \langle \mathcal{N}^2 M_{\text{ap}} \rangle(\theta_1, \theta_2, \theta_3) + i \langle \mathcal{N}^2 M_{\perp} \rangle(\theta_1, \theta_2, \theta_3) \\ &= \frac{1}{N^2} \int d^2\vartheta_1 \int d^2\vartheta_2 \int d^2\vartheta_3 U_{\theta_1}(\boldsymbol{\vartheta}_1) U_{\theta_2}(\boldsymbol{\vartheta}_2) Q_{\theta_3}(\boldsymbol{\vartheta}_3) \\ & \quad \langle N(\boldsymbol{\vartheta}_1) N(\boldsymbol{\vartheta}_2) [\gamma_t(\boldsymbol{\vartheta}_3) + i \gamma_\times(\boldsymbol{\vartheta}_3)] \rangle. \end{aligned} \quad (12)$$

These aperture statistics can be related to $\tilde{\mathcal{G}}$ for a chosen filter function U_θ . Provided the exponential filter function,

$$U_\theta(\boldsymbol{\vartheta}) = \frac{1}{2\pi\theta^2} \left(1 - \frac{\vartheta^2}{2\theta^2} \right) \exp\left(-\frac{\vartheta^2}{2\theta^2}\right), \quad (13)$$

Schneider & Watts (2005) found

$$\begin{aligned} \langle \mathcal{N}^2 M_{\text{ap}} \rangle(\theta_1, \theta_2, \theta_3) &= \int_0^\infty d\vartheta_1 \vartheta_1 \int_0^\infty d\vartheta_2 \vartheta_2 \int_0^{2\pi} d\phi \\ & \quad \tilde{\mathcal{G}}(\boldsymbol{\vartheta}_1, \boldsymbol{\vartheta}_2, \phi) A_{\mathcal{N}\mathcal{N}M}(\boldsymbol{\vartheta}_1, \boldsymbol{\vartheta}_2, \phi | \theta_1, \theta_2, \theta_3), \end{aligned} \quad (14)$$

with the kernel function $A_{\mathcal{N}\mathcal{N}M}(\boldsymbol{\vartheta}_1, \boldsymbol{\vartheta}_2, \phi | \theta_1, \theta_2, \theta_3)$ in the appendix of Schneider & Watts (2005).

As discussed in Schneider (2003), the imaginary part of the integral in equation (14), the B-mode $\langle \mathcal{N}^2 M_{\perp} \rangle$, is expected to vanish, unless systematic effects cause a parity violation. We do not expect such a violation by any physical process; even the occurrence of B-modes for the gravitational shear, which might be due to intrinsic alignments or clustering of source galaxies (Schneider et al. 2002), cannot induce a non-zero $\langle \mathcal{N}^2 M_{\perp} \rangle$. We nevertheless measure $\langle \mathcal{N}^2 M_{\perp} \rangle$, as a consistency check alongside the E-mode $\langle \mathcal{N}^2 M_{\text{ap}} \rangle$ with $\tilde{\mathcal{G}}_{\text{est}}$. We only measure the aperture statistics for equal aperture scale radii θ and use the short-hands $\langle \mathcal{N}^2 M_{\text{ap}} \rangle(\theta, \theta, \theta) =: \langle \mathcal{N}^2 M_{\text{ap}} \rangle(\theta)$ and $\langle \mathcal{N}^2 M_{\perp} \rangle(\theta, \theta, \theta) =: \langle \mathcal{N}^2 M_{\perp} \rangle(\theta)$.

3. Methods

3.1. Redshift weighting

To reduce the signal degradation by uncorrelated lens pairs, we define a redshift-weighted correlation function $\tilde{\mathcal{G}}_Z$, for which lens pairs are weighted according to their redshift difference δz . To that end we introduce the redshift weighting function $Z(\delta z)$ for which we choose a Gaussian,

$$Z(\delta z) = \exp\left(-\frac{\delta z^2}{2\sigma_Z^2}\right). \quad (15)$$

The width σ_Z is a free parameter that should correspond to the typical redshift difference of correlated lens pairs. The weighting function is normalized such that it is unity, if the galaxies have the same redshift. Averaging over the tangential ellipticities of lens-lens-source triplets weighted with Z leads to an estimate of

$$\frac{\int d\mathbf{z}_1 \int d\mathbf{z}_2 Z(\Delta z_{12}) \langle N(\boldsymbol{\vartheta}_1 + \boldsymbol{\theta}, z_1) N(\boldsymbol{\vartheta}_2 + \boldsymbol{\theta}, z_2) \gamma_t(\boldsymbol{\vartheta}_3 + \boldsymbol{\theta}) \rangle}{\int d\mathbf{z}_1 \int d\mathbf{z}_2 Z(\Delta z_{12}) \langle N(\boldsymbol{\vartheta}_1 + \boldsymbol{\theta}, z_1) N(\boldsymbol{\vartheta}_2 + \boldsymbol{\theta}, z_2) \rangle} \quad (16)$$

$$=: \frac{\tilde{\mathcal{G}}_Z(\boldsymbol{\vartheta}_1, \boldsymbol{\vartheta}_2, \phi)}{1 + \omega_Z(|\boldsymbol{\vartheta}_1 - \boldsymbol{\vartheta}_2|)},$$

where $N(\boldsymbol{\vartheta}, z)$ is the number density of lens galaxies at angular position $\boldsymbol{\vartheta}$ and redshift z , and $\Delta z_{12} = z_1 - z_2$. Equation (16) defines the redshift-weighted correlation function $\tilde{\mathcal{G}}_Z$ and uses the redshift-weighted two-point angular correlation function ω_Z . We estimate $\tilde{\mathcal{G}}_Z$ with

$$\begin{aligned} \tilde{\mathcal{G}}_{Z,\text{est}}(b) &= - \frac{\sum_{ijk} w_k \epsilon_k e^{-i(\varphi_i + \varphi_j)} [1 + \omega_Z(|\boldsymbol{\theta}_i - \boldsymbol{\theta}_j|)] Z(\Delta z_{ij}) \Delta_{ijk}(b)}{\sum_{ijk} w_k Z(\Delta z_{ij}) \Delta_{ijk}(b)}. \end{aligned} \quad (17)$$

For estimating the redshift-weighted two-point correlation ω_Z , we use the N_r randoms, located at $\boldsymbol{\theta}'_i$, the N_d lenses at the positions $\boldsymbol{\theta}_i$, and the estimator

$$\omega_Z(\theta) = \frac{N_r^2 DD_Z(\theta)}{N_d^2 RR_Z(\theta)} - 2 \frac{N_r DR_Z(\theta)}{N_d RR_Z(\theta)} + 1, \quad (18)$$

with the modified paircounts

$$\begin{aligned} DD_Z(\theta) &= \sum_{i=1}^{N_d} \sum_{j=1}^{N_d} \Theta_{\text{H}}(\theta + \Delta\theta/2 - |\boldsymbol{\theta}_i - \boldsymbol{\theta}_j|) \\ & \quad \Theta_{\text{H}}(-\theta + \Delta\theta/2 + |\boldsymbol{\theta}_i - \boldsymbol{\theta}_j|) Z(\Delta z_{ij}), \end{aligned} \quad (19)$$

$$\begin{aligned} RR_Z(\theta) &= \sum_{i=1}^{N_r} \sum_{j=1}^{N_r} \Theta_{\text{H}}(\theta + \Delta\theta/2 - |\boldsymbol{\theta}_i - \boldsymbol{\theta}_j|) \\ & \quad \Theta_{\text{H}}(-\theta + \Delta\theta/2 + |\boldsymbol{\theta}'_i - \boldsymbol{\theta}'_j|) Z(\Delta z_{ij}), \end{aligned} \quad (20)$$

and

$$\begin{aligned} DR_Z(\theta) &= \sum_{i=1}^{N_d} \sum_{j=1}^{N_r} \Theta_{\text{H}}(\theta + \Delta\theta/2 - |\boldsymbol{\theta}'_i - \boldsymbol{\theta}'_j|) \\ & \quad \Theta_{\text{H}}(-\theta + \Delta\theta/2 + |\boldsymbol{\theta}'_i - \boldsymbol{\theta}'_j|) Z(\Delta z_{ij}). \end{aligned} \quad (21)$$

Here, Θ_{H} is the Heaviside step function and $\Delta\theta$ is the bin size for which ω_Z is estimated. For $Z \equiv 1$, this estimator reduces to the standard Landy–Szalay estimator in Eq. (7).

The aperture statistics from the redshift weighted correlation function $\tilde{\mathcal{G}}_Z$ are expected to have a higher SNR than the aperture statistics from the original $\tilde{\mathcal{G}}$. This expected improvement can be estimated with simplified assumptions. For this, we assume that the N_{tot} lens-lens-source triplets can be split into N_{true} physical triplets, each carrying the signal s , and $N_{\text{tot}} - N_{\text{true}}$ triplets carrying no signal. We further assume, that all triplets carry the same uncorrelated noise n . Then, the measured total signal S , noise N and SNR S/N are

$$S = \frac{N_{\text{true}}}{N_{\text{tot}}} s, \quad N = \frac{1}{\sqrt{N_{\text{tot}}}} n, \quad \text{and } S/N = \frac{N_{\text{true}}}{\sqrt{N_{\text{tot}}}} \frac{s}{n}. \quad (22)$$

With redshift weighting we decrease the effective number of triplets from N_{tot} to \tilde{N}_{tot} , while retaining the same number of physical triplets N_{true} . The signal \tilde{S} , the noise \tilde{N} and the SNR \tilde{S}/\tilde{N} are then

$$\tilde{S} = \frac{N_{\text{true}}}{\tilde{N}_{\text{tot}}} s, \quad \tilde{N} = \frac{1}{\sqrt{\tilde{N}_{\text{tot}}}} n, \quad \text{and} \quad \tilde{S}/\tilde{N} = \frac{N_{\text{true}}}{\sqrt{\tilde{N}_{\text{tot}}}} \frac{s}{n}. \quad (23)$$

Consequently, redshift weighting increases the noise by a factor of $(N_{\text{tot}}/\tilde{N}_{\text{tot}})^{1/2}$. Nonetheless, the SNR improves by $(N_{\text{tot}}/\tilde{N}_{\text{tot}})^{1/2}$, since the signal increases by $N_{\text{tot}}/\tilde{N}_{\text{tot}}$. Accordingly, we expect the SNR to increase approximately by the square root of the signal increase.

The critical parameter for the redshift weighting is the width σ_z of the weighting function. For our application on the observational and simulated data described in Sect. 4, we choose $\sigma_z = 0.01$. As there is no clear dividing line between lens pairs that carry signal and those that do not, the choice of this parameter needs to remain somewhat arbitrary. However, three arguments can be made to motivate our choice.

The first considers the galaxy correlation length. [Farrow et al. \(2015\)](#) measured the two-point correlation function of galaxies in the Galaxy and Mass Assembly survey (GAMA) and found correlation lengths between $3.28 \pm 0.42 h^{-1}$ Mpc and $38.17 \pm 0.47 h^{-1}$ Mpc, depending on the galaxies' stellar masses. The same function was measured by [Zehavi et al. \(2011\)](#) in the Sloan Digital Sky Survey, who found similar correlation lengths between $4.2 h^{-1}$ Mpc and $10.5 h^{-1}$ Mpc. These correlation lengths correspond to redshift differences between 0.001 and 0.005 at the median redshift of GAMA of $z = 0.21$. We assume that galaxies separated by more than twice the correlation length are only weakly correlated, and therefore our choice of $\sigma_z = 0.01$ seems appropriate.

The second argument relates to the distribution of lens galaxy pairs with their redshift difference. The blue histogram in Fig. 2 shows the number of galaxy pairs per redshift difference δz with fixed angular separation between $4'5$ and $5'5$ in our lens sample from the MR (see Sect. 4). This distribution has a prominent peak for small δz and a broad background distribution. Thus, most galaxy pairs that appear close on the sky are also close in redshift space. These physical pairs make up the peak. However, the background distribution shows that there are also many galaxy pairs with small angular separation, whose redshift difference is large. The redshift weighting function should now be chosen in such a way that pairs inside the peak are preserved, while the background is suppressed.

The other histograms in Fig. 2 show different weighted distributions, where the number of galaxy pairs is multiplied by the redshift weighting function from Eq. (15). This gives the effective number of galaxy pairs per redshift difference bin that are considered for the improved $\tilde{\mathcal{G}}$ estimator. Here, the effect of different σ_z is visible. Using $\sigma_z = 0.1$ and 0.05 preserves the peak, but a large fraction of background is still present in the weighted distribution. For $\sigma_z = 0.005$ and $\sigma_z = 0.001$, the background is removed but parts of the peak are also suppressed. A middle ground is found for $\sigma_z = 0.01$. Here, the tails of the peak still contribute, while most of the background galaxy pairs are suppressed. Consequently, we adopt this value for the measurement of $\tilde{\mathcal{G}}$ and subsequently $\langle \mathcal{N}^2 M_{\text{ap}} \rangle$.

The third argument for our choice of σ_z considers the peculiar velocities of galaxies in clusters, which can cause redshift differences of correlated galaxy pairs inside the same halo. The weighting function Z needs to be broad enough, that galaxy pairs with redshift differences induced simply by their peculiar motion

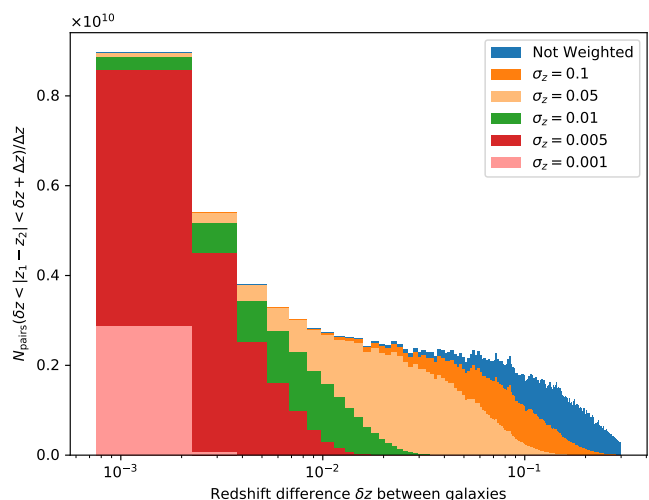


Fig. 2: Weighted number of lens galaxy pairs in our sample from the MR with fixed angular separation between $4'5$ and $5'5$ per redshift difference between the pairs. Different colours indicate different widths of the Gaussian weighting function. The blue histogram shows the unweighted distribution, the green histogram shows the distribution with the weighting chosen for the G3L measurements.

should not be discarded. Velocities of galaxies inside halos can reach up to 1000 km s^{-1} , leading to redshift differences of up to 0.006. This is a lower bound for σ_z , so choosing $\sigma_z = 0.01$ appears valid.

3.2. New Binning Scheme

In previous work ([Simon et al. 2008, 2013](#)), $\tilde{\mathcal{G}}$ was measured on a regular grid, which had logarithmic spacing in the lens-source separations ϑ_1 and ϑ_2 and linear spacing in the opening angle ϕ . The aperture statistics are then calculated by summing over this grid.

However, this approach has a drawback. Due to the finite number of galaxy triplets, some bins contain no triplets. In these bins, the estimator for $\tilde{\mathcal{G}}$ is undefined and was set to zero in previous work. This effect occurs both for small triangle sides ϑ_1 and ϑ_2 , as for these the bin size is smaller, and for large triangle sides, as the finite field size makes the occurrence of larger triangles improbable. Furthermore, for a square field-of-view, certain bins automatically remain empty for ϑ_1 or ϑ_2 larger than the side length of the field-of-view, as ϕ is restricted and cannot have all values between 0 and 2π . As a result, $\langle \mathcal{N}^2 M_{\text{ap}} \rangle$ is underestimated both at small and large scales. A discussion of this bias is provided in [Simon et al. \(2008\)](#).

To account for this effect, we introduce a new binning scheme, illustrated in Fig. 3. Here $\tilde{\mathcal{G}}$ is first estimated on a regular grid, together with the average side lengths of the triplets in each bin. Then, in all bins for which triplets are found, the measured $\tilde{\mathcal{G}}$ is associated with the average ϑ_1 , ϑ_2 and ϕ of the corresponding bin. Using the averages of the triplets in filled bins as seeds, the parameter space is divided by a Voronoi tessellation, using the library `voro++` by [Rycroft \(2009\)](#). Each Voronoi cell is then considered as a new bin for which $\tilde{\mathcal{G}}$ is estimated. The aperture statistics are obtained by integrating over the N_{bin} new

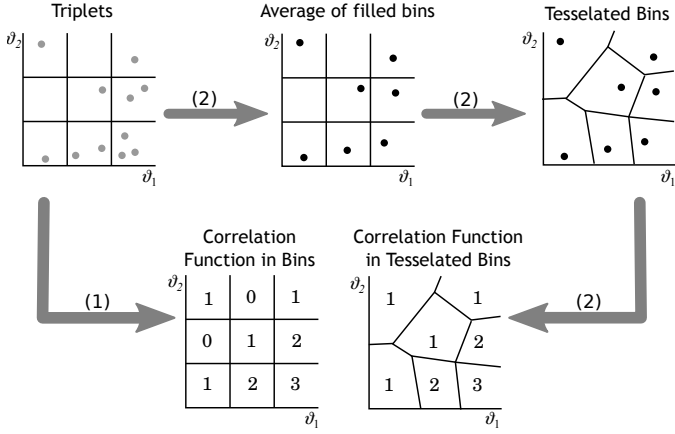


Fig. 3: Illustration of the old (1) and new (2) binning scheme for the calculation of $\tilde{\mathcal{G}}$. In the old binning scheme, $\tilde{\mathcal{G}}$ was calculated directly from the lens-lens-source triplets inside a given bin. In the new binning scheme, first the average of the lens-lens-source triplets in a bin are calculated. These averages are used as seeds for a Voronoi tessellation of the parameter space. Each Voronoi cell is then considered as a new bin for which $\tilde{\mathcal{G}}$ is estimated. The aperture statistics are obtained by integrating over the new bins. In this figure only two dimensions are shown, but for the measurement the tessellation is also done along the third parameter ϕ .

bins, using the numerical approximation of Eq. (14),

$$\langle \mathcal{N}^2 M_{\text{ap}} \rangle(\theta) + i \langle \mathcal{N}^2 M_{\perp} \rangle(\theta) = \sum_{i=1}^{N_{\text{bin}}} V(b_i) \tilde{\mathcal{G}}_{\text{est}}(b_i) A_{NNM}(b_i|\theta), \quad (24)$$

where b_i is the i th bin, $V(b_i)$ is the volume of this bin and $A_{NNM}(b_i|\theta)$ is the kernel function of Eq. (14) evaluated at the seed of b_i . We estimate $\tilde{\mathcal{G}}$ on a grid with $128 \times 128 \times 128$ bins with ϑ_1 and ϑ_2 between $0'.15$ and $320'$ for the data based on the MR (see Sect. 4.1) and between $0'.15$ and $200'$ for the simple mock data (see Sect. 4.2). The tessellation reduces the number of bins by approximately 3 % in both cases.

3.3. Conversion to physical units

With the lens redshifts z_1 and z_2 , we can transform the projected angular separation vectors $\boldsymbol{\vartheta}_1$ and $\boldsymbol{\vartheta}_2$ into physical separations \mathbf{r}_1 and \mathbf{r}_2 on a plane midway between the two lenses, using

$$\mathbf{r}_{1,2} = D_A(0, z_{12}) \boldsymbol{\vartheta}_{1,2} =: D_A(z_{12}) \boldsymbol{\vartheta}_{1,2}, \quad (25)$$

with the angular diameter distance $D_A(z_a, z_b)$ between redshifts z_a and z_b and the average lens redshift $z_{12} = (z_1 + z_2)/2$.

The correlation function $\tilde{\mathcal{G}}_Z$ can therefore be estimated in physical scales in the bin b of r_1 , r_2 and ϕ as

$$\tilde{\mathcal{G}}_{Z,\text{est}}(b) = - \frac{\sum_{ijk} w_k \epsilon_k e^{-i(\varphi_i + \varphi_j)} \left[1 + \omega(|\boldsymbol{\theta}_i - \boldsymbol{\theta}_j|) \right] Z(\Delta z_{ij}) \Delta_{ijk,\text{ph}}(b)}{\sum_{ijk} w_k Z(\Delta z_{ij}) \Delta_{ijk,\text{ph}}(b)}, \quad (26)$$

with

$$\Delta_{ijk,\text{ph}}(b) \quad (27)$$

$$= \begin{cases} 1 & \text{for } (D_A(z_{ij})|\boldsymbol{\theta}_k - \boldsymbol{\theta}_i|, D_A(z_{ij})|\boldsymbol{\theta}_k - \boldsymbol{\theta}_j|, \phi_{ijk}) \in b \\ 0 & \text{otherwise} \end{cases}$$

This $\tilde{\mathcal{G}}_Z$ still depends on the redshift distribution of sources, as the gravitational shear γ_t depends on the lensing efficiency, which in turn depends on the observer-source and lens-source distances. Hence, to compare the measurements of different surveys with varying source redshift distributions it is useful to correlate the galaxy number density not with the tangential shear γ_t , but instead with the projected excess mass density $\Delta\Sigma$, given by

$$\Delta\Sigma(\boldsymbol{\theta}, z_d, z_s) = \begin{cases} \frac{\gamma_t(\boldsymbol{\theta})}{\Sigma_{\text{crit}}^{-1}(z_d, z_s)} & \text{for } z_d < z_s, \\ 0 & \text{else} \end{cases}, \quad (28)$$

with the inverse critical surface mass density

$$\Sigma_{\text{crit}}^{-1}(z_d, z_s) = \frac{4\pi G}{c^2} \frac{D_A(z_d, z_s) D_A(z_d)}{D_A(z_s)} \Theta_H(z_s - z_d). \quad (29)$$

Thus, we are interested in the correlation function $\tilde{\mathcal{G}}_{\text{phys}}$, defined by

$$\begin{aligned} \tilde{\mathcal{G}}_{\text{phys}}(\mathbf{r}_1, \mathbf{r}_2) &= \frac{1}{N^2} \int dz_1 \int dz_2 p(z_1) p(z_2) Z(\Delta z_{12}) \\ &\left\langle N\left(\frac{\mathbf{r}_1}{D_A(z_{12})} + \boldsymbol{\theta}, z_1\right) N\left(\frac{\mathbf{r}_2}{D_A(z_{12})} + \boldsymbol{\theta}, z_2\right) \Delta\Sigma(\boldsymbol{\theta}) \right\rangle \\ &=: \tilde{\mathcal{G}}_{\text{phys}}(r_1, r_2, \phi). \end{aligned} \quad (30)$$

To estimate this quantity with a maximum likelihood estimator, we need to multiply the weight w_k of each source galaxy with $\Sigma_{\text{crit}}^{-2}$ (Sheldon et al. 2004). This leads to the estimator

$$\begin{aligned} \tilde{\mathcal{G}}_{\text{est,phys}}(b) &= (-1) \times \\ &\frac{\sum_{ijk} w_k \epsilon_k e^{-i(\varphi_i + \varphi_j)} \left[1 + \omega(|\boldsymbol{\theta}_i - \boldsymbol{\theta}_j|) \right] Z(\Delta z_{ij}) \Sigma_{\text{crit}}^{-1}(z_{ij}, z_k) \Delta_{ijk,\text{ph}}(b)}{\sum_{ijk} w_k \Sigma_{\text{crit}}^{-2}(z_{ij}, z_k) Z(\Delta z_{ij}) \Delta_{ijk,\text{ph}}(b)}. \end{aligned} \quad (31)$$

This estimator requires a precise knowledge of the source redshifts. For the application to real data though, often only photometric redshift estimates are available for source galaxies. Therefore, we do not use the exact $\Sigma_{\text{crit}}^{-1}$ for each triplet, but instead $\bar{\Sigma}_{\text{crit}}^{-1}$, which is averaged over the source distribution $p_s(z_s)$ as

$$\bar{\Sigma}_{\text{crit}}^{-1}(z_d) = \int dz_s p_s(z_s) \Sigma_{\text{crit}}^{-1}(z_d, z_s). \quad (32)$$

Consequently, we estimate $\tilde{\mathcal{G}}_{\text{phys}}$ with

$$\begin{aligned} \tilde{\mathcal{G}}_{\text{est,phys}}(b) &= (-1) \times \\ &\frac{\sum_{ijk} w_k \epsilon_k e^{-i(\varphi_i + \varphi_j)} \left[1 + \omega(|\boldsymbol{\theta}_i - \boldsymbol{\theta}_j|) \right] Z(\Delta z_{ij}) \bar{\Sigma}_{\text{crit}}^{-1}(z_{ij}) \Delta_{ijk,\text{ph}}(b)}{\sum_{ijk} w_k \bar{\Sigma}_{\text{crit}}^{-2}(z_{ij}) Z(\Delta z_{ij}) \Delta_{ijk,\text{ph}}(b)}. \end{aligned} \quad (33)$$

We convert this physical three-point correlation function to physical aperture statistics with

$$\begin{aligned} &\langle \mathcal{N}^2 M_{\text{ap}} \rangle_{\text{phys}}(R) + i \langle \mathcal{N}^2 M_{\perp} \rangle_{\text{phys}}(R) \\ &= \int_0^{\infty} dr_1 r_1 \int_0^{\infty} dr_2 r_2 \int_0^{2\pi} d\phi \\ &\tilde{\mathcal{G}}_{\text{phys}}(r_1, r_2, \phi) A_{NNM}(D_A^{-1}(z_{12}) r_1, D_A^{-1}(z_{12}) r_2, \phi | D_A^{-1}(z_{12}) R). \end{aligned} \quad (34)$$

These aperture statistics are in units of mass over area.

3.4. Magnification of lens galaxies

Magnification of lens galaxies by the LSS affects G3L, as the apparent magnitude and number density of lenses is changed (Bartelmann & Schneider 2001). In the weak lensing limit, the number density of lens galaxies at angular position $\boldsymbol{\theta}$ and redshift z is changed from the intrinsic number density $N_0(\boldsymbol{\theta}, z)$ to

$$N(\boldsymbol{\theta}, z) = N_0(\boldsymbol{\theta}, z) + 2[\alpha(z) - 1] \bar{N} \kappa(\boldsymbol{\theta}, z), \quad (35)$$

where $\kappa(\boldsymbol{\theta}, z)$ is the convergence caused by all matter in front of redshift z , and $\alpha(z)$ is the negative slope of the luminosity function $\Phi(S, z)$ at the flux limit S_{lim} of lens galaxies. We define α by

$$\alpha = -\frac{d \ln \Phi}{d \ln S}(S_{\text{lim}}). \quad (36)$$

Consequently, the correlation function $\tilde{\mathcal{G}}_Z$ with the impact of lens magnification is

$$\begin{aligned} \tilde{\mathcal{G}}_Z(\boldsymbol{\theta}_1, \boldsymbol{\theta}_2, \phi) = & \int dz_1 \int dz_2 Z(z_1 - z_2) \\ & \left\{ \frac{1}{\bar{N}^2} \langle N_0(\boldsymbol{\theta}_1 + \boldsymbol{\theta}, z_1) N_0(\boldsymbol{\theta}_2 + \boldsymbol{\theta}, z_2) \gamma_t(\boldsymbol{\theta}) \rangle \right. \\ & + \frac{2[\alpha(z_2) - 1]}{\bar{N}} \langle N_0(\boldsymbol{\theta}_1 + \boldsymbol{\theta}, z_1) \kappa(\boldsymbol{\theta}_2 + \boldsymbol{\theta}, z_2) \gamma_t(\boldsymbol{\theta}) \rangle \\ & + \frac{2[\alpha(z_1) - 1]}{\bar{N}} \langle \kappa(\boldsymbol{\theta}_1 + \boldsymbol{\theta}, z_1) N_0(\boldsymbol{\theta}_2 + \boldsymbol{\theta}, z_2) \gamma_t(\boldsymbol{\theta}) \rangle \\ & \left. + \frac{4([\alpha(z_1) - 1][\alpha(z_2) - 1]}{\bar{N}} \langle \kappa(\boldsymbol{\theta}_1 + \boldsymbol{\theta}, z_1) \kappa(\boldsymbol{\theta}_2 + \boldsymbol{\theta}, z_2) \gamma_t(\boldsymbol{\theta}) \rangle \right\}. \end{aligned} \quad (37)$$

With the intrinsic aperture number count

$$\mathcal{N}_{0,\theta}(\boldsymbol{\theta}, z) = \frac{1}{\bar{N}} \int d^2 \boldsymbol{\theta}' U_\theta(|\boldsymbol{\theta} - \boldsymbol{\theta}'|) N_0(\boldsymbol{\theta}', z), \quad (38)$$

and $M_{\text{ap},\theta}$ as defined in Eq. (9), the aperture statistics are

$$\begin{aligned} \langle \mathcal{N}^2 M_{\text{ap}} \rangle(\theta) = & \int dz_1 \int dz_2 Z(z_1 - z_2) \\ & \left\{ \langle \mathcal{N}_{0,\theta}(\boldsymbol{\theta}, z_1) \mathcal{N}_{0,\theta}(\boldsymbol{\theta}, z_2) M_{\text{ap},\theta}(\boldsymbol{\theta}) \rangle \right. \\ & + 2[\alpha(z_2) - 1] \langle \mathcal{N}_{0,\theta}(\boldsymbol{\theta}, z_1) M_{\text{ap},\theta}(\boldsymbol{\theta}, z_2) M_{\text{ap},\theta}(\boldsymbol{\theta}) \rangle \\ & + 2[\alpha(z_1) - 1] \langle M_{\text{ap},\theta}(\boldsymbol{\theta}, z_1) \mathcal{N}_{0,\theta}(\boldsymbol{\theta}, z_2) M_{\text{ap},\theta}(\boldsymbol{\theta}) \rangle \\ & \left. + 4[\alpha(z_1) - 1][\alpha(z_2) - 1] \langle M_{\text{ap},\theta}(\boldsymbol{\theta}, z_1) M_{\text{ap},\theta}(\boldsymbol{\theta}, z_2) M_{\text{ap},\theta}(\boldsymbol{\theta}) \rangle \right\}. \end{aligned} \quad (39)$$

Thus, the measured aperture statistics do not include only the intrinsic first term, but three additional terms due to lens magnification. These lens magnification terms, though, can be measured by using as redshift weighting function Z not a Gaussian, but a step function,

$$Z(z_1 - z_2) = \Theta_H(z_2 - z_1 - \Delta z). \quad (40)$$

This means, that only lens pairs with a redshift difference larger than Δz and $z_2 > z_1$ are counted in the estimator in Eq. (17). As explained in Sect. 3.1, we expect lens pairs with redshift differences larger than 0.01 to be intrinsically uncorrelated. Hence, if

we choose $\Delta z = 0.01$, the first term in Eq. (39), which contains only the correlation of intrinsic number densities, should vanish. The measured $\langle \mathcal{N}^2 M_{\text{ap}} \rangle$ is then purely the correlation due to the lens magnification. We measure this $\langle \mathcal{N}^2 M_{\text{ap}} \rangle$ with the estimator in Eq. (17), using the step function weighting. If this signal is then subtracted from the measured $\langle \mathcal{N}^2 M_{\text{ap}} \rangle$ of all lenses, we obtain the intrinsic aperture statistics.

As we are testing our approach on simulated data from the MR, for which both the number density and convergence are available at different redshift planes, we can also use another approach to measure the terms due to lens magnification. In this approach we use that the observed aperture number count \mathcal{N}_θ is related to the intrinsic aperture number count $\mathcal{N}_{0,\theta}$ and aperture mass $M_{\text{ap},\theta}$ via

$$\mathcal{N}_\theta(\boldsymbol{\theta}, z) = \frac{1}{\bar{N}} \int d^2 \boldsymbol{\theta}' U_\theta(|\boldsymbol{\theta} - \boldsymbol{\theta}'|) N(\boldsymbol{\theta}', z) \quad (41)$$

$$= \mathcal{N}_{0,\theta} + 2[\alpha(z) - 1] M_{\text{ap},\theta}(\boldsymbol{\theta}, z). \quad (42)$$

Consequently, Eq. (39) with the step function weighting in Eq. (40) leads to

$$\begin{aligned} \langle \mathcal{N}^2 M_{\text{ap}} \rangle(\theta) = & \int_0^{z_{\text{max}}} dz_1 \int_{z_1 + \Delta z}^{z_{\text{max}}} dz_2 \\ & \left\{ \langle \mathcal{N}_{0,\theta}(\boldsymbol{\theta}, z_1) \mathcal{N}_{0,\theta}(\boldsymbol{\theta}, z_2) M_{\text{ap},\theta}(\boldsymbol{\theta}) \rangle \right. \\ & + 2[\alpha(z_2) - 1] \langle \mathcal{N}_\theta(\boldsymbol{\theta}, z_1) M_{\text{ap},\theta}(\boldsymbol{\theta}, z_2) M_{\text{ap},\theta}(\boldsymbol{\theta}) \rangle \\ & + 2[\alpha(z_1) - 1] \langle M_{\text{ap},\theta}(\boldsymbol{\theta}, z_1) \mathcal{N}_\theta(\boldsymbol{\theta}, z_2) M_{\text{ap},\theta}(\boldsymbol{\theta}) \rangle \\ & \left. - 4[\alpha(z_1) - 1][\alpha(z_2) - 1] \langle M_{\text{ap},\theta}(\boldsymbol{\theta}, z_1) M_{\text{ap},\theta}(\boldsymbol{\theta}, z_2) M_{\text{ap},\theta}(\boldsymbol{\theta}) \rangle \right\}, \end{aligned} \quad (43)$$

where the terms due to lens magnification are given by the observed, rather than the intrinsic aperture number count. For a numerical evaluation, the integrals can be converted into sums over M redshift slices, so

$$\begin{aligned} \langle \mathcal{N}^2 M_{\text{ap}} \rangle(\theta) & = \sum_{i=0}^M \sum_{j=i+1}^M \Delta z_i \Delta z_j \left\{ \langle \mathcal{N}_{0,\theta}(\boldsymbol{\theta}, z_i) \mathcal{N}_{0,\theta}(\boldsymbol{\theta}, z_j) M_{\text{ap},\theta}(\boldsymbol{\theta}) \rangle \right. \\ & + 2[\alpha(z_j) - 1] \langle \mathcal{N}_\theta(\boldsymbol{\theta}, z_i) M_{\text{ap},\theta}(\boldsymbol{\theta}, z_j) M_{\text{ap},\theta}(\boldsymbol{\theta}) \rangle \\ & + 2[\alpha(z_i) - 1] \langle M_{\text{ap},\theta}(\boldsymbol{\theta}, z_i) \mathcal{N}_\theta(\boldsymbol{\theta}, z_j) M_{\text{ap},\theta}(\boldsymbol{\theta}) \rangle \\ & \left. - 4[\alpha(z_i) - 1][\alpha(z_j) - 1] \langle M_{\text{ap},\theta}(\boldsymbol{\theta}, z_i) M_{\text{ap},\theta}(\boldsymbol{\theta}, z_j) M_{\text{ap},\theta}(\boldsymbol{\theta}) \rangle \right\} \\ & =: \sum_{i=0}^M \sum_{j=i+1}^M \Delta z_i \Delta z_j \langle \mathcal{N}_{0,\theta}(\boldsymbol{\theta}, z_i) \mathcal{N}_{0,\theta}(\boldsymbol{\theta}, z_j) M_{\text{ap},\theta}(\boldsymbol{\theta}) \rangle \\ & + L_{NMM}(\theta) + L_{MNM}(\theta) + L_{MMM}(\theta). \end{aligned} \quad (44)$$

Using Eq. (45), we measure the lens magnification terms L_{MMM} , L_{MNM} and L_{NMM} directly in the simulated data based on the MR for $z_j < 0.5$ and $z_i < z_j$.

For this, we first convolve the number density and convergence maps at each redshift plane with the filter function U_θ to obtain $\mathcal{N}_\theta(\boldsymbol{\theta}, z_i)$ and $M_{\text{ap},\theta}(\boldsymbol{\theta}, z_j)$. We then multiply the aperture statistics for each combination of z_i and z_j and spatially average the products to obtain $\langle \mathcal{N}_\theta(\boldsymbol{\theta}, z_i) M_{\text{ap},\theta}(\boldsymbol{\theta}, z_j) M_{\text{ap},\theta}(\boldsymbol{\theta}) \rangle$ and $\langle M_{\text{ap},\theta}(\boldsymbol{\theta}, z_i) M_{\text{ap},\theta}(\boldsymbol{\theta}, z_j) M_{\text{ap},\theta}(\boldsymbol{\theta}) \rangle$. These averages are then multiplied by the appropriate α and summed over. We repeat this procedure for different aperture scale radii θ between 0.5 and $8'$.

Table 1: Slopes $\alpha(z)$ of the luminosity function at different redshifts z in the MR. The limiting magnitude of galaxies is $r_{\text{lim}} = 19.8$ mag.

z	$\alpha(z)$
0.46	2.51
0.41	2.38
0.36	2.01
0.32	1.80
0.28	1.36
0.24	1.15
0.21	0.91
0.17	0.78
0.14	0.49
0.12	0.48
0.09	0.48
0.06	0.47
0.04	0.17

For this calculation, the slope $\alpha(z)$ of the lens luminosity function needs to be known. To obtain $\alpha(z)$, we extract the luminosity function $\Phi(S, z)$ at each redshift plane of the MR, with S measured in the r -band filter. We then fit a power law to $\Phi(S, z)$ in the proximity of the limiting flux. This flux is given in our case by the limiting r -band magnitude, chosen to be $r_{\text{lim}} = 19.8$ mag. The slopes for each redshift z are the $\alpha(z)$ given in Table 1.

4. Data

4.1. Simulated data based on the MR

We test our new estimator with simulated data sets from the MR. The MR (Springel et al. 2005) is a dark matter-only cosmological N-body-simulation. It traces the evolution of 2160^3 dark matter particles of mass $m = 8.6 \times 10^8 h^{-1} M_{\odot}$ from redshift $z = 127$ to today in a cubic region with co-moving side length $500 h^{-1}$ Mpc. For this, a flat Λ CDM cosmology is assumed, with matter density $\Omega_m = 0.25$, baryon density $\Omega_b = 0.045$, dark energy density $\Omega_{\Lambda} = 0.75$, Hubble constant $H_0 = 73 \text{ km s}^{-1} \text{ Mpc}^{-1}$ and power spectrum normalization $\sigma_8 = 0.9$.

Maps of the complex gravitational shear $\gamma = \gamma_1 + i\gamma_2$, caused by the matter distribution in the MR, are created with the multiple-lens-plane ray-tracing algorithm by Hilbert et al. (2009). With this algorithm, 64 maps of γ on a regular mesh with 4096^2 pixels, corresponding to $4 \times 4 \text{ deg}^2$ on a set of redshift planes are created. For each field-of-view, we combine the shear on nine redshift planes between $z = 0.5082$ and $z = 1.1734$ by adding the shearm weighted by an assumed source redshift distribution $p_s(z)$. This redshift distribution, shown in Fig. 4 is modelled after the redshift distribution of galaxies in the Kilo-Degree Survey (KiDS; Wright et al. 2018; Hildebrandt et al. 2018). To mimic the shape noise in observational data, we add a random number drawn from a Gaussian probability distribution to both shear components at each pixel. The standard deviation of this Gaussian is set to 0.3.

Lens galaxies in the simulation are created by using the SAM by H15. It is one of various SAMs that have been implemented on the MR (see e.g. Guo et al. 2011; Bower et al. 2006), but as Saghiiha et al. (2017) have shown, this model agrees particularly well with measurements of GGL and G3L in CFHTLenS. To simulate the selection function of observations, we apply a redshift and flux limit on our lens samples. We use lenses with $z \leq 0.5$ and SDSS r -band magnitude brighter than 19.8

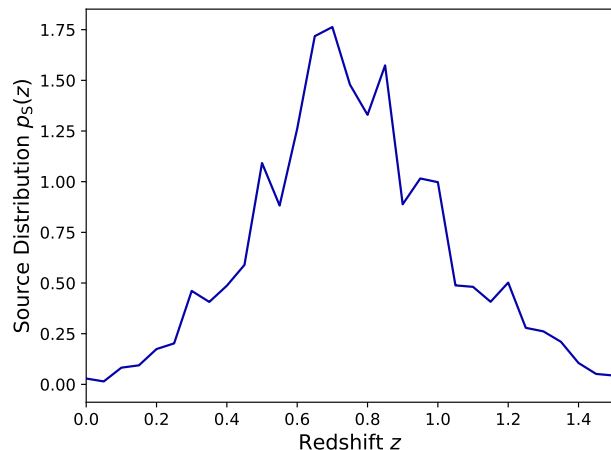


Fig. 4: Assumed source redshift distribution. This distribution is used to weigh the shear maps at different redshifts in the MR. It is modelled after the redshift distribution of galaxies in Hildebrandt et al. (2018).

mag. With these limits, we obtain a number density of lenses of $0.282 \text{ arcmin}^{-2}$.

The total number of triplets to consider for our measurement of $\tilde{\mathcal{G}}_Z$ and $\tilde{\mathcal{G}}_{\text{phys}}$ is 5×10^{12} . This makes the evaluation of the sums in Eq. (17) and Eq. (33) computationally involved. Due to this computational complexity, third-order correlation functions are usually computed involving some approximation, such as kd-Tree codes (Simon et al. 2013), where galaxy triplets with similar ϑ_1, ϑ_2 and ϕ are averaged. However, we implement the estimator brute-force and calculate it with Graphics Processing Units (GPUs). This approach has two advantages compared to the usual methods involving some approximation to reduce the computational complexity, such as kd-Tree codes (Simon et al. 2013):

- It is exact, even at smallest scales.
- The computing time is drastically reduced, due to the highly parallelized execution on a GPU, where several thousand calculations can be done simultaneously.

In our case, the computational time to process the MR decreases from 200 hours with a kd-Tree code executed on 8 CPU cores to just 9 hours with the brute force code on a single GPU. Details to our computational implementation are given in App. B.

The covariance matrices of the measured $\langle \mathcal{N}^2 M_{\text{ap}} \rangle$ and $\langle \mathcal{N}^2 M_{\text{ap}} \rangle_{\text{phys}}$ are computed with jackknifing. For this, we assume each of the 64 fields is an independent realization and combine these fields to a total $\langle \mathcal{N}^2 M_{\text{ap}} \rangle(\theta)$ and 64 jackknife samples $\langle \mathcal{N}^2 M_{\text{ap}} \rangle_k(\theta)$ where all but the k th tile are combined. The covariance matrix is then

$$C(\theta_i, \theta_j) = \frac{64}{64-1} \sum_{k=1}^{64} \left[\langle \mathcal{N}^2 M_{\text{ap}} \rangle_k(\theta_i) - \overline{\langle \mathcal{N}^2 M_{\text{ap}} \rangle_k}(\theta_i) \right] \times \left[\langle \mathcal{N}^2 M_{\text{ap}} \rangle_k(\theta_j) - \overline{\langle \mathcal{N}^2 M_{\text{ap}} \rangle_k}(\theta_j) \right], \quad (46)$$

where $\overline{\langle \mathcal{N}^2 M_{\text{ap}} \rangle_k}(\theta_i)$ is the average of all $\langle \mathcal{N}^2 M_{\text{ap}} \rangle_k(\theta_i)$. The statistical uncertainty of $\langle \mathcal{N}^2 M_{\text{ap}} \rangle(\theta_i)$ is $\sigma_i = \sqrt{C(\theta_i, \theta_i)}$.

4.2. Simple mock data

Some of our tests also employ simple mock data. These are chosen such, that it is both easy to create them and to calculate their expected aperture statistics theoretically. For this we use the following assumptions.

- A. All matter and galaxies are distributed inside N_h halos over an area A .
- B. All halos are situated on the same lens plane.
- C. All halos have the same axisymmetric convergence profile $\kappa(\vartheta) = K u(\vartheta)$, where $\int d\vartheta \vartheta u(\vartheta) = 1$, as well as the same number of galaxies N_{gal} .
- D. There is no galaxy bias, so the discrete galaxy distribution follows the matter distribution up to Poisson shot-noise.
- E. Halo centres are distributed randomly within A .

With these assumptions and the calculations in App. A, the theoretical expectation for the aperture statistics using the exponential filter function in Eq. (13) is

$$\begin{aligned} & \langle \mathcal{N}^2 M_{\text{ap}} \rangle (\theta_1, \theta_2, \theta_3) \\ &= \frac{2\pi A K}{N_h} \int_0^\infty d\vartheta \vartheta \prod_{i=1}^3 \int_0^\infty dy_i \frac{y_i u(y_i)}{\theta_i^2} \exp\left[-\frac{(y_i - \vartheta)^2}{2\theta_i^2}\right] \\ & \left[\left(1 - \frac{y_i^2 + \vartheta^2}{2\theta_i^2}\right) f_0\left(\frac{y_i \vartheta}{\theta_i^2}\right) + \frac{y_i \vartheta}{\theta_i^2} f_1\left(\frac{y_i \vartheta}{\theta_i^2}\right) \right], \end{aligned} \quad (47)$$

with $f_n(x) = I_n(x) e^{-x}$ and the modified Bessel functions of the first kind $I_n(x)$. We evaluate the integrals numerically with a Monte-Carlo integration using the monte-vegas-routine of the GNU Scientific Library (Gough 2009).

As halo convergence profile $\kappa(\vartheta)$, we use the Brainerd-Blandford-Smail (BBS) profile (Brainerd et al. 1996), which is

$$\kappa(\vartheta) = \frac{K}{2\pi \vartheta \theta_s} \left(1 - \frac{\vartheta}{\sqrt{\vartheta^2 + \theta_s^2}}\right). \quad (48)$$

The BBS profile corresponds to a singular isothermal sphere (SIS) for ϑ much smaller than the scale radius θ_s , while smoothly dropping outside. In contrast to the SIS profile, it has a finite total mass. We choose $K = 1 \text{ arcmin}^2$ and $\theta_s = 5'$.

We create mock lens galaxies following assumptions A to E in a circular area with a radius of $700'$. The lens galaxies are distributed in 2170 halos with 200 galaxies each. These numbers are chosen such, that the average number density of lens galaxies is $\bar{N}_d = 0.287 \text{ arcmin}^{-2}$, the lens number density in our lens sample from the MR. We distribute 3×10^6 source galaxies, whose shears are computed from the halo convergence profiles, in the central $750 \times 750 \text{ arcmin}^2$ area. We only consider lens-lens-source triplets in this area, to ensure that the shear of each source is impacted by halos from all directions. No shape noise is added to the shears, as we do not want to create a realistic simulation, but only a simple test case. As $\tilde{\mathcal{G}}$ is linear in the ellipticities, any shape noise would not bias its estimate and only lead to a larger uncertainty of the measurement. The central area is cut into 25 quadratic tiles with a side length of $150'$, so that uncertainties can be estimated with jackknifing.

5. Results

5.1. Impact of new binning scheme

Before measuring the aperture statistics in the data based on the MR, we estimate the effect of the new binning scheme, by measuring the aperture statistics for equal scale radii θ in the simple

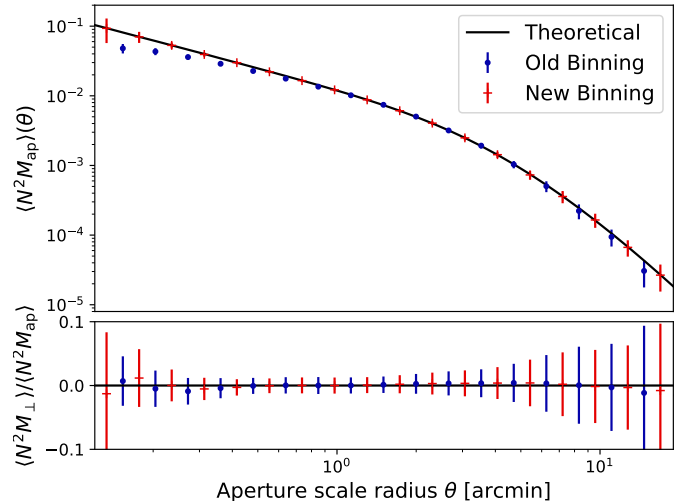


Fig. 5: Aperture statistics measured in the simple mock data with the old binning scheme (blue dots) and the new binning scheme (red crosses) as well as the theoretical expectation (black line) given by Eq. (47). The upper plot shows the E-mode $\langle \mathcal{N}^2 M_{\text{ap}} \rangle$ while the lower plot shows the ratio of the B-mode $\langle \mathcal{N}^2 M_{\perp} \rangle$ and the E-mode. Uncertainties are the statistical error estimated with jackknifing.

mock data, described in Sect 4.2. The aperture statistics measured in this mock data are displayed in Fig. 5. The theoretically expected $\langle \mathcal{N}^2 M_{\text{ap}} \rangle$ follows a power law for scale radii above $2'$ and steepens for larger scales. The $\langle \mathcal{N}^2 M_{\text{ap}} \rangle$ measured with the old and the new binning scheme both show the same steepening for θ larger than $2'$, but the slope of the $\langle \mathcal{N}^2 M_{\text{ap}} \rangle$ measured with the old binning scheme is considerably shallower for scales between $0.1'$ and $0.6'$ than the one measured with the new binning scheme. We confirm that the measurement with the new binning scheme agrees with the theoretical expectation within its statistical uncertainty. This agreement of the measured aperture statistics with the theoretical prediction validates our code to estimate $\tilde{\mathcal{G}}$ and to convert $\tilde{\mathcal{G}}$ to $\langle \mathcal{N}^2 M_{\text{ap}} \rangle$.

To quantify the impact of the new binning scheme, Fig. 6 shows the difference of the measured $\langle \mathcal{N}^2 M_{\text{ap}} \rangle$ to the theoretical prediction for both binning schemes, normalized by the theoretical prediction. While the $\langle \mathcal{N}^2 M_{\text{ap}} \rangle$ from the old method has no bias at scales between $1'$ and $5'$, it underestimates $\langle \mathcal{N}^2 M_{\text{ap}} \rangle$ both above and below these scales. At large scales, this bias grows to 10% at $\theta = 10'$, whereas at small scales, the bias increases with decreasing scale to be 40% at $\theta = 0.1'$. The new binning scheme does not show this behaviour. Instead, the bias of the $\langle \mathcal{N}^2 M_{\text{ap}} \rangle$ measured with the new method is consistent with zero at all considered scales.

5.2. Impact of lens magnification

As outlined in Sect. 3.4, the redshift weighting enables us to measure the impact of lens magnification on G3L. We estimate this effect in the data based on the MR with the two different methods outlined in Sect 3.4.

The result for the first method, using the step function weighting in the estimation of $\tilde{\mathcal{G}}_Z$, is shown in Figs. 7 and 8 for

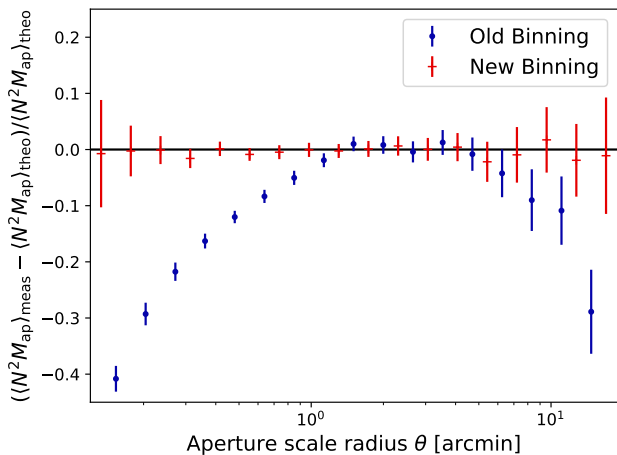


Fig. 6: Fractional difference of the measured $\langle \mathcal{N}^2 M_{\text{ap}} \rangle$ relative to the theoretical prediction in the mock data. Blue dots show the measurement with the old binning scheme; red crosses show the measurement with the new binning scheme.

$\langle \mathcal{N}^2 M_{\text{ap}} \rangle$ and $\langle \mathcal{N}^2 M_{\text{ap}} \rangle_{\text{phys}}$, respectively. The figures show the aperture statistics measured for lens pairs with redshift differences larger than 0.01. If there was no lens magnification, this signal should vanish. As reference, the figures also show the aperture statistics measured when taking into account all lens pairs, as well as the intrinsic aperture statistics “corrected” for the impact of lens magnification by subtracting the signal of physically distant lens pairs from the total measured aperture statistics.

For both $\langle \mathcal{N}^2 M_{\text{ap}} \rangle$ and $\langle \mathcal{N}^2 M_{\text{ap}} \rangle_{\text{phys}}$, the signal of physically separated lens pairs is non-zero. We attribute this signal to the three magnification terms in Eq. (39). For $\langle \mathcal{N}^2 M_{\text{ap}} \rangle$ this signal is approximately 10% of the signal of all lens pairs. For $\langle \mathcal{N}^2 M_{\text{ap}} \rangle_{\text{phys}}$, the magnification leads to a slightly smaller additional signal at scales below $0.1 h^{-1}$ Mpc and approximately 10% at larger scales.

At angular scales smaller than $0'.2$, the signal due to lens magnification for $\langle \mathcal{N}^2 M_{\text{ap}} \rangle$ decreases. This is probably due to smoothing in the simulation, which is not accurate any more at these small angular scales. Smoothing flattens the centre of halo convergence profiles in the simulation. If the aperture statistics are measured at scale radii smaller than the smoothing lengths, the flattened profile then leads to a smaller measured signal.

To verify that the measured signal for distant lens pairs is indeed related to lens magnification, Fig. 9 shows the magnification terms measured with the second method from Sect. 3.4, using the convolution of the aperture filter function with the convergence and number density maps. In comparison, the measured $\langle \mathcal{N}^2 M_{\text{ap}} \rangle$ from the first method is also shown.

The figure shows that $L_{NMM}(\theta)$, which is due to the correlation of the number density of galaxies at smaller redshift to the convergence measured at higher redshifts, is the dominating term. It is larger than L_{MMM} and L_{MNM} by three orders of magnitude. Furthermore, the correlation of three convergence maps L_{MMM} and the correlation of foreground convergence maps to background galaxies L_{MNM} are almost identical. Consequently, the total lens magnification signal is approximately L_{NMM} .

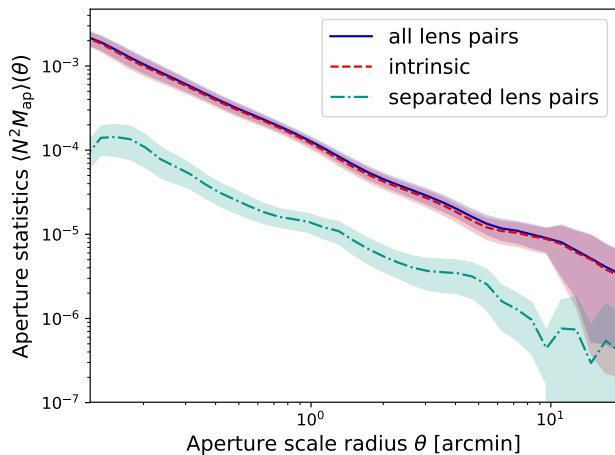


Fig. 7: Impact of magnification bias on aperture statistics in the data based on the MR. The green, dash-dotted line shows the signal measured for lens pairs with redshift differences larger than 0.01, which corresponds to the magnification terms in Eq. (39). The blue solid line is the aperture statistics for all lens pairs. The red dashed line is the intrinsic signal, which is corrected for lens magnification by subtracting the signal of separated lens pairs. Shaded regions are the 1σ uncertainties from jackknifing.

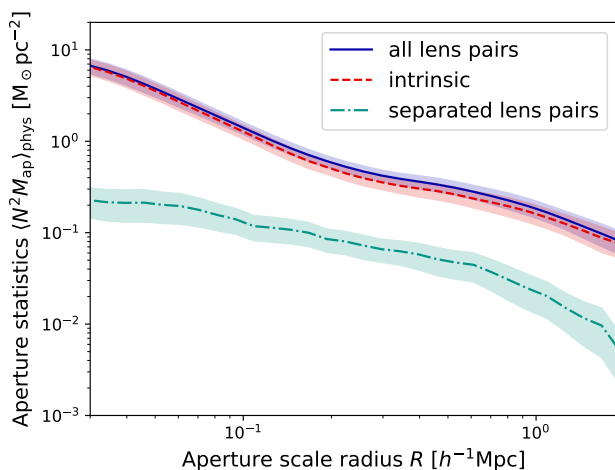


Fig. 8: Same as Fig. 7, but for physical aperture statistics.

This indicates that the lens magnification signal is driven mainly by the correlation of matter and the galaxy distribution at the first lens plane. This matter affects the convergence at the second lens and the source plane and thereby causes a significant L_{NMM} . Both L_{MNM} and L_{MMM} do not depend on the correlation between matter and galaxies at the same plane and are mainly caused by the LSS in front of the first lens plane. This LSS influences \mathcal{N}_θ and $M_{\text{ap},\theta}$ at both lens planes and the source plane and thereby induces the non-zero L_{MNM} and L_{MMM} . However, as shown in Fig. 9, this effect is secondary, and the LSS in front of the lenses does not have a large impact on the overall signal.

The total lens magnification signal is of the same order of magnitude as the $\langle \mathcal{N}^2 M_{\text{ap}} \rangle$ measured with separated lens pairs. Indeed, at scales above $1'$ it agrees with the measured $\langle \mathcal{N}^2 M_{\text{ap}} \rangle$

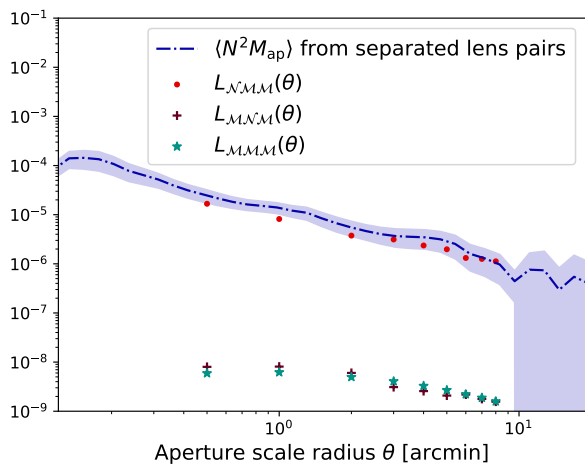


Fig. 9: Individual lens magnification terms in the MR. Green stars depict the term due to correlation between the convergence maps at the two lens planes and at the source plane, red dots are the term due to correlation of the galaxy number density at the first lens plane to the convergence maps at the second lens- and the source plane, brown crosses are the term due to correlation of the convergence maps at the first lens- and the source plane to the galaxy number density at the second lens plane. The blue line is the measured $\langle \mathcal{N}^2 M_{\text{ap}} \rangle$ for separated lens pairs, which should correspond to the total lens magnification signal.

for separated lens pairs within its statistical uncertainty. At smaller scales, the difference between the two quantities is still smaller than twice the statistical uncertainty. Due to Eq. (43), the intrinsic aperture statistics are

$$\begin{aligned} & \langle \mathcal{N}_{0,\theta}(\boldsymbol{\vartheta}, z_1) \mathcal{N}_{0,\theta}(\boldsymbol{\vartheta}, z_2) M_{\text{ap},\theta}(\boldsymbol{\vartheta}) \rangle \\ &= \langle \mathcal{N}^2 M_{\text{ap}} \rangle(\theta) - L_{NMM}(\theta) - L_{MNM}(\theta) - L_{MMM}(\theta), \end{aligned} \quad (49)$$

where $\langle \mathcal{N}^2 M_{\text{ap}} \rangle$ are the measured aperture statistics for separated lens pairs. Therefore, the intrinsic aperture statistics for separated lens pairs vanishes as expected.

5.3. Impact of redshift weighting

The results for $\langle \mathcal{N}^2 M_{\text{ap}} \rangle$ for the data based on the MR with and without redshift weighting are shown in Fig. 10a. The measured $\langle \mathcal{N}^2 M_{\perp} \rangle$ is consistent with zero, both with and without redshift weighting. This signifies that no indication of parity violation and B-modes is found in the simulation.

Redshift weighting increases the SNR, as indicated by the decreasing error region in Fig. 10a. Simultaneously, the measured $\langle \mathcal{N}^2 M_{\text{ap}} \rangle$ is increased by a factor of approximately two. This is expected, since redshift weighting is supposed to increase both signal and SNR, as discussed in Sect. 3.1. The lower plot in Fig. 10a shows the SNR of $\langle \mathcal{N}^2 M_{\text{ap}} \rangle$ with and without redshift weighting as function of the aperture scale radius θ . Redshift weighting increases the SNR on all scales. On average, the SNR of $\langle \mathcal{N}^2 M_{\text{ap}} \rangle$ with redshift weighting is 1.35 times the SNR of $\langle \mathcal{N}^2 M_{\text{ap}} \rangle$ without redshift weighting.

The measured physical aperture statistics $\langle \mathcal{N}^2 M_{\text{ap}} \rangle_{\text{phys}}$ are displayed in Fig. 10b. Again, the B-mode is consistent with zero

at all scales. Redshift weighting increases the signal by a factor of two, similar to the increase of $\langle \mathcal{N}^2 M_{\text{ap}} \rangle$, while the error region decreases. The increase of the SNR of $\langle \mathcal{N}^2 M_{\text{ap}} \rangle_{\text{phys}}$, shown in the lower plot of Fig. 10b, is at the same level as for $\langle \mathcal{N}^2 M_{\text{ap}} \rangle$; on average, the SNR increases by 34%. In Fig. 10, one also notices that the SNR of $\langle \mathcal{N}^2 M_{\text{ap}} \rangle_{\text{phys}}$ is higher than the SNR of $\langle \mathcal{N}^2 M_{\text{ap}} \rangle$, both with and without redshift weighting.

6. Discussion

In this work, we proposed three improvements to the measurement of the G3L signal: Using a redshift weighting of lens galaxies to improve the precision, removing biases on the estimator with a new binning scheme and accounting for the impact of lens magnification. We further showed how to measure the G3L signal in physical units.

The impact of the improved binning scheme can be seen by comparing our measurement on the simple mock data with the theoretical expectation. While the original binning leads to a discrepancy between the theoretical expectation and the measurement both for aperture scale radii below $1'$ and above $5'$, the aperture statistics measured with the improved binning agrees with the expectation at all scales. At $\theta = 0.1$, the original binning underestimates $\langle \mathcal{N}^2 M_{\text{ap}} \rangle$ by 40%, whereas the result of the new binning scheme agrees with the theoretical expectation. Thus, our new method extends the reliability of the measurement. This is achieved by the tessellation, as now the three-point correlation function is not falsely set to zero in bins for which no lens-lens-source triplet is found.

The signal due to magnification of lens galaxies is approximately 10% of the total G3L signal and can therefore not be neglected in theoretical modelling of the G3L signal. Previous studies (Simon et al. 2008, 2013) did not account for lens magnification. Nonetheless, even though it has a significant impact on the measured G3L signal, the conclusions of (Saghiha et al. 2017), who found good agreement between the G3L measured in CFHTLenS and the MR with the SAM by H15, are not impaired by this, as both the observational data and the simulations included lens magnification.

We also demonstrated how to correct for the impact of lens magnification. The additional signal due to this effect can be measured with our redshift weighting, by considering only lens pairs sufficiently separated along the line-of-sight. The resulting signal matches the expectation for lens magnification from the convergence and number density maps at different redshift slices. We therefore conclude that the lens magnification signal can indeed be measured by using physically separated lens pairs, which have no intrinsic correlation. As lens magnification only causes an additive signal, the intrinsic correlation can be found by subtracting the additional component from the overall measurement.

By the direct measurement of the different terms due to lens magnification, we found that the dominating term is caused by correlation of galaxies at the closer lens plane to the convergence measured at the second lens plane and the convergence measured at the source plane, whereas the other terms are three orders of magnitude smaller. This finding explains why we measure a significant signal due to lens magnification, even though previous studies (e.g. Simon et al. 2013) expected this effect to be negligible: In those evaluations, only the M_{ap}^3 -term was considered, which indeed is much smaller than any $\langle \mathcal{N}^2 M_{\text{ap}} \rangle$ signal. How-

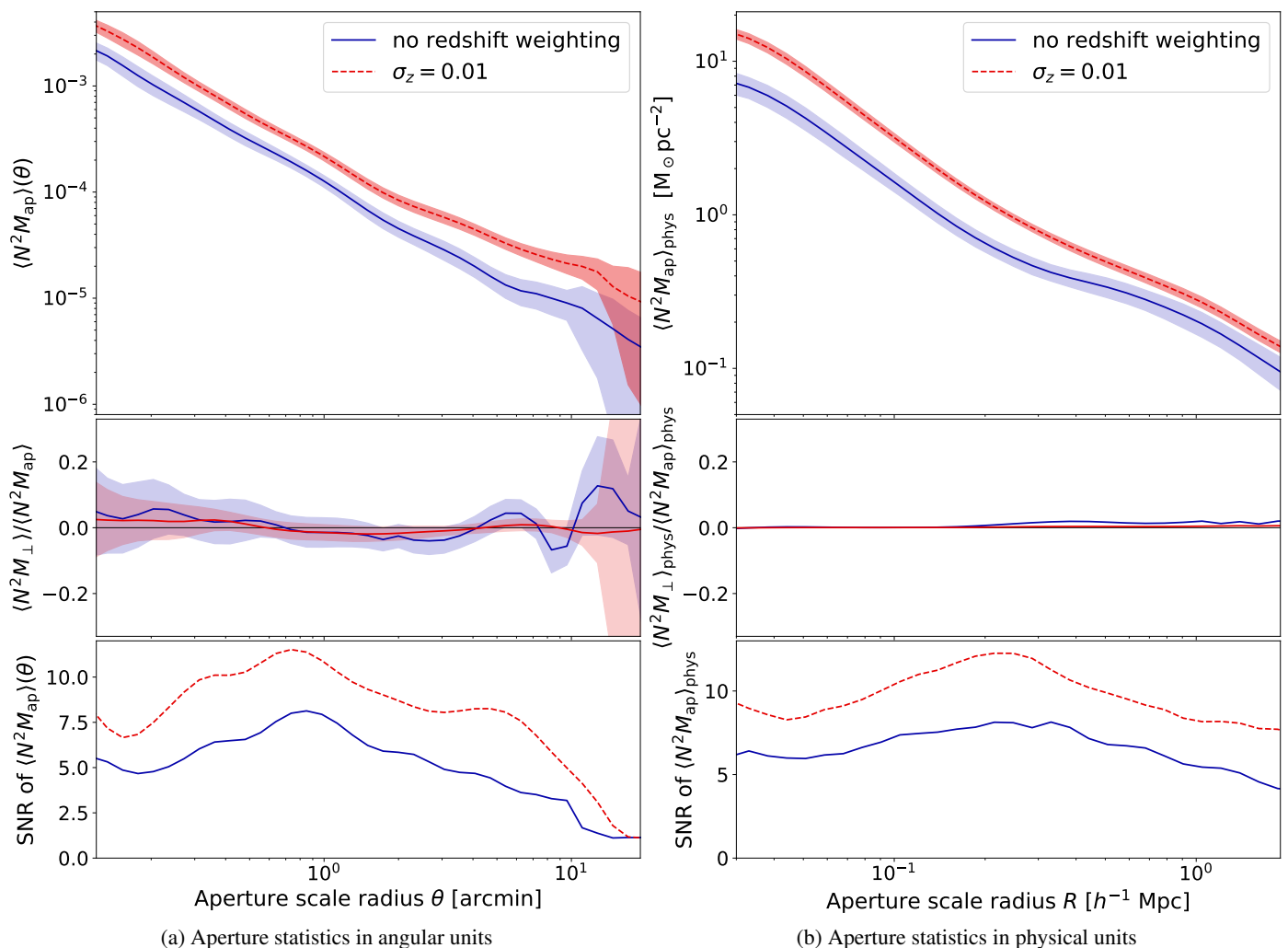


Fig. 10: Aperture statistics measured in the mock data based on the MR, in (a) with angular and in (b) with physical units. The upper plots show the E-modes $\langle \mathcal{N}^2 M_{\text{ap}} \rangle$ and $\langle \mathcal{N}^2 M_{\text{ap}} \rangle_{\text{phys}}$, while the middle plot shows the ratio of the B-modes $\langle \mathcal{N}^2 M_{\perp} \rangle$ and $\langle \mathcal{N}^2 M_{\perp} \rangle_{\text{phys}}$ to $\langle \mathcal{N}^2 M_{\text{ap}} \rangle$ and $\langle \mathcal{N}^2 M_{\text{ap}} \rangle_{\text{phys}}$. The lower plots give the SNR of $\langle \mathcal{N}^2 M_{\text{ap}} \rangle$ and $\langle \mathcal{N}^2 M_{\text{ap}} \rangle_{\text{phys}}$. Shaded regions show the 1σ uncertainties from jackknifing. The blue solid line denote the measurements without redshift weighting. The red dashed line depicts $\langle \mathcal{N}^2 M_{\text{ap}} \rangle$ taken with a redshift weighting function with width $\sigma_z = 0.01$.

ever, as we have shown here, it is not the dominant term for lens magnification.

The magnification signal is mainly due to correlation of galaxies with matter at the first lens plane, which influences the convergence at the second lens and the source plane. Matter in front of both lenses, which influences the observed lens number density and the convergence at both lens and the source plane also contribute to the magnification signal, although its measured contribution is minor. Nonetheless, as our lens sample is quite shallow and has a low median redshift of 0.2, the impact of foreground matter might be larger for lens samples at higher redshifts.

Using redshift weighting, we increased the SNR of both $\langle \mathcal{N}^2 M_{\text{ap}} \rangle$ and $\langle \mathcal{N}^2 M_{\text{ap}} \rangle_{\text{phys}}$ by approximately 35% between 0.1 and $10'$ and $0.1h^{-1}\text{Mpc}$ and $2h^{-1}\text{Mpc}$. Simultaneously, the signal is increased by a factor of approximately two. This fits to our expectation, that the signal increases by the square of the increase in SNR.

Our choice of σ_z was motivated by the correlation length between galaxies, the redshift distribution of galaxy pairs and the typical peculiar velocities of galaxies in clusters. Choosing a different σ_z will lead both to a different measured signal and a different increase in SNR. However, the choice of σ_z does not impact the physical interpretation of the aperture statistics, as long as the same σ_z is chosen in the theoretical modelling. Moreover, for each survey different values of σ_z can be chosen and the one which provides the best SNR increase can be retained.

For the redshift weighting scheme in the MR, we could use exact redshifts for all lens galaxies. This is generally not possible for observations. While the redshift weighting with a broad weighting function might be possible for lens galaxies with photometric redshift estimates, we expect that redshift weighting will be most useful for data sets including spectroscopic redshifts. The uncertainties of spectroscopic redshifts are much smaller than of photometric redshifts, so a narrow weighting function, such as the one chosen for this work, can be used.

At first glance, the measurement of the aperture statistics in physical units $\langle \mathcal{N}^2 M_{\text{ap}} \rangle_{\text{phys}}$ does not appear to provide additional information to the measurement in angular units. However, we stress that this quantity, in contrast to $\langle \mathcal{N}^2 M_{\text{ap}} \rangle$ is independent of the source redshift distribution. Direct comparisons of $\langle \mathcal{N}^2 M_{\text{ap}} \rangle_{\text{phys}}$ between surveys with different galaxy distributions are possible. Furthermore, the SNR of $\langle \mathcal{N}^2 M_{\text{ap}} \rangle_{\text{phys}}$ is slightly higher than for $\langle \mathcal{N}^2 M_{\text{ap}} \rangle$, independent of the redshift weighting. This is because for $\langle \mathcal{N}^2 M_{\text{ap}} \rangle_{\text{phys}}$, triplets are weighted according to their lensing efficiency.

Here, we have only applied our improvements on the lens-lens-shear correlation function and the aperture statistics $\langle \mathcal{N}^2 M_{\text{ap}} \rangle$. However, the new binning scheme can also be applied to measurements of the lens-shear-shear correlation and $\langle \mathcal{N} M_{\text{ap}}^2 \rangle$. We suspect that this could extend the accuracy of measurement of this aperture statistics to scales below $1'$, which were not taken into account in previous measurements (Simon et al. 2013). The transformation into physical units can also be applied for $\langle \mathcal{N} M_{\text{ap}}^2 \rangle$.

Acknowledgements. We thank Sandra Unruh for providing code for the slopes of the galaxy luminosity function in the MR. LL is a member of and received financial support for this research from the International Max Planck Research School (IMPRS) for Astronomy and Astrophysics at the Universities of Bonn and Cologne.

References

- Bard, D., Bellis, M., Allen, M. T., Yepremyan, H., & Kratochvil, J. M. 2013, *Astronomy and Computing*, 1, 17
- Bartelmann, M. & Schneider, P. 2001, *Phys. Rep.*, 340, 291
- Bower, R. G., Benson, A. J., Malbon, R., et al. 2006, *MNRAS*, 370, 645
- Brainerd, T. G., Blandford, R. D., & Smail, I. 1996, *ApJ*, 466, 623
- Cárdenas-Montes, M., Rodríguez-Vázquez, J. J., Vega-Rodríguez, M. A., Sevilla-Noarbe, I., & Alvaro, E. S. 2014, *Computer Physics Communications*, 185, 2558
- Clampitt, J., Miyatake, H., Jain, B., & Takada, M. 2016, *MNRAS*, 457, 2391
- Crain, R. A., Schaye, J., Bower, R. G., et al. 2015, *MNRAS*, 450, 1937
- Farrow, D. J., Cole, S., Norberg, P., et al. 2015, *MNRAS*, 454, 2120
- Gough, B. 2009, *GNU Scientific Library Reference Manual - Third Edition*, 3rd edn. (Network Theory Ltd.)
- Guo, Q., White, S., Boylan-Kolchin, M., et al. 2011, *MNRAS*, 413, 101
- Henriques, B. M. B., White, S. D. M., Thomas, P. A., et al. 2015, *MNRAS*, 451, 2663
- Hilbert, S., Hartlap, J., White, S. D. M., & Schneider, P. 2009, *A&A*, 499, 31
- Hildebrandt, H., Köhlinger, F., van den Busch, J. L., et al. 2018, *arXiv e-prints*, arXiv:1812.06076
- Hildebrandt, H., Viola, M., Heymans, C., et al. 2017, *MNRAS*, 465, 1454
- Lacey, C. G., Baugh, C. M., Frenk, C. S., et al. 2016, *MNRAS*, 462, 3854
- Landy, S. D. & Szalay, A. S. 1993, *ApJ*, 412, 64
- Mandelbaum, R., Hirata, C. M., Broderick, T., Seljak, U., & Brinkmann, J. 2006, *MNRAS*, 370, 1008
- Mead, J. M. G., King, L. J., & McCarthy, I. G. 2010, *MNRAS*, 401, 2257
- Planck Collaboration, Ade, P. A. R., Aghanim, N., et al. 2016, *A&A*, 594, A13
- Rycroft, C. H. 2009, *Chaos: An Interdisciplinary Journal of Nonlinear Science*, 19, 041111
- Saghiha, H., Simon, P., Schneider, P., & Hilbert, S. 2017, *A&A*, 601, A98
- Schneider, P. 2003, *A&A*, 408, 829
- Schneider, P., van Waerbeke, L., & Mellier, Y. 2002, *A&A*, 389, 729
- Schneider, P. & Watts, P. 2005, *A&A*, 432, 783
- Sheldon, E. S., Johnston, D. E., Frieman, J. A., et al. 2004, *AJ*, 127, 2544
- Simon, P., Erben, T., Schneider, P., et al. 2013, *MNRAS*, 430, 2476
- Simon, P. & Hilbert, S. 2018, *A&A*, 613, A15
- Simon, P., Saghiha, H., Hilbert, S., et al. 2019, *A&A*, 622, A104
- Simon, P., Watts, P., Schneider, P., et al. 2008, *A&A*, 479, 655
- Springel, V., White, S. D. M., Jenkins, A., et al. 2005, *Nature*, 435, 629
- Vogelsberger, M., Genel, S., Springel, V., et al. 2014, *MNRAS*, 444, 1518
- Wright, A. H., Hildebrandt, H., Kuijken, K., et al. 2018, *arXiv e-prints*, arXiv:1812.06077
- Zehavi, I., Zheng, Z., Weinberg, D. H., et al. 2011, *ApJ*, 736, 59

Appendix A: Calculation of aperture statistics for mock data

Averages in the halo model are given by

$$\langle f \rangle = \int dm_1 \dots dm_{N_h} \underbrace{P_m(m_1, \dots, m_{N_h})}_{\text{Probability that haloes have masses } m_1, \dots, m_2} \quad (\text{A.1})$$

$$\int d^3 x_1 \dots d^3 x_{N_h} \underbrace{P_h(\mathbf{x}_1, \dots, \mathbf{x}_{N_h} \mid m_1, \dots, m_{N_h})}_{\text{Probability that halo centers are at } \mathbf{x}_1, \dots, \mathbf{x}_{N_h}}$$

$$\int d^3 \Delta \mathbf{x}_{11} \dots \int d^3 \Delta \mathbf{x}_{N_h N_{\text{gal}}} \underbrace{P_{\text{gal}}(\Delta \mathbf{x}_{11}, \dots, \Delta \mathbf{x}_{N_h N_{\text{gal}}} \mid \mathbf{x}_1, \dots, \mathbf{x}_{N_h}, m_1, \dots, m_{N_h})}_{\text{Probability that galaxies are at } \Delta \mathbf{x}_{11}, \dots, \Delta \mathbf{x}_{N_h N_{\text{gal}}} \text{ if the halos are at } \boldsymbol{\vartheta}_1, \dots, \boldsymbol{\vartheta}_{N_h}} f .$$

Using assumption B in Sect. 5.1, we can reduce this integration to two spatial dimensions and use the projected halo centres $\boldsymbol{\vartheta}_i$ and the projected separation $\Delta \boldsymbol{\vartheta}_{ij}$ of the j th galaxy to the i th halo centre instead of \mathbf{x}_i and $\Delta \mathbf{x}_{ij}$. Furthermore, due to assumption C the mass integrals are trivial. Assumption D leads to

$$P_{\text{gal}}(\Delta \boldsymbol{\vartheta}_{11}, \dots, \Delta \boldsymbol{\vartheta}_{N_h N_{\text{gal}}} \mid \boldsymbol{\vartheta}_1, \dots, \boldsymbol{\vartheta}_{N_h}, m_1, \dots, m_{N_h}) = \quad (\text{A.2})$$

$$= u(\Delta \boldsymbol{\vartheta}_{11}) \dots u(\Delta \boldsymbol{\vartheta}_{N_h N_{\text{gal}}}) .$$

Assumption E means that

$$P_h(\boldsymbol{\vartheta}_1, \dots, \boldsymbol{\vartheta}_{N_h}) = \begin{cases} A^{-N_h} & \text{for } (\boldsymbol{\vartheta}_1, \dots, \boldsymbol{\vartheta}_{N_h}) \in A \\ 0 & \text{else} \end{cases} , \quad (\text{A.3})$$

so the average of a quantity is given by

$$\langle f \rangle = A^{-N_h} \int_A d^2 \boldsymbol{\vartheta}_1 \dots d^2 \boldsymbol{\vartheta}_{N_h} \int d^2 \Delta \boldsymbol{\vartheta}_{11} \dots d^2 \Delta \boldsymbol{\vartheta}_{N_h N_{\text{gal}}} \quad (\text{A.4})$$

$$u_1(\Delta \boldsymbol{\vartheta}_{11}) \dots u_{N_h}(\Delta \boldsymbol{\vartheta}_{N_h N_{\text{gal}}}) f .$$

Consequently, the correlation function $\langle N(\boldsymbol{\theta}_1) N(\boldsymbol{\theta}_2) \kappa(\boldsymbol{\theta}_3) \rangle$ of the galaxy number density $N(\boldsymbol{\theta})$ and the projected matter density κ is

$$\langle N(\boldsymbol{\theta}_1) N(\boldsymbol{\theta}_2) \kappa(\boldsymbol{\theta}_3) \rangle \quad (\text{A.5})$$

$$= A^{-N_h} \int_A d^2 \boldsymbol{\vartheta}_1 \dots d^2 \boldsymbol{\vartheta}_{N_h} \int d^2 \Delta \boldsymbol{\vartheta}_{11} \dots d^2 \Delta \boldsymbol{\vartheta}_{N_h N_{\text{gal}}}$$

$$u_1(\Delta \boldsymbol{\vartheta}_{11}) \dots u_{N_h}(\Delta \boldsymbol{\vartheta}_{N_h N_{\text{gal}}}) N(\boldsymbol{\theta}_1) N(\boldsymbol{\theta}_2) \kappa(\boldsymbol{\theta}_3) .$$

The matter density κ is the sum of the convergence profiles of all halos,

$$\kappa(\boldsymbol{\theta}) = K \sum_{i=1}^{N_h} u(|\boldsymbol{\theta} - \boldsymbol{\vartheta}_i|) . \quad (\text{A.6})$$

We treat galaxies as discrete objects, so their number density is

$$N(\boldsymbol{\theta}) = \sum_{i=1}^{N_h} \sum_{j=1}^{N_{\text{gal}}} \delta_{\text{D}}(\boldsymbol{\theta} - \boldsymbol{\vartheta}_i - \Delta \boldsymbol{\vartheta}_{ij}) . \quad (\text{A.7})$$

Inserting Eq. (A.6) and Eq. (A.7) into Eq. (A.5) leads to

$$\langle N(\boldsymbol{\theta}_1) N(\boldsymbol{\theta}_2) \kappa(\boldsymbol{\theta}_3) \rangle \quad (\text{A.8})$$

$$= A^{-N_h} K \int_A d^2 \boldsymbol{\vartheta}_1 \dots d^2 \boldsymbol{\vartheta}_{N_h} \int d^2 \Delta \boldsymbol{\vartheta}_{11} \dots d^2 \Delta \boldsymbol{\vartheta}_{N_h N_{\text{gal}}}$$

$$u_1(\Delta \boldsymbol{\vartheta}_{11}) \dots u_{N_h}(\Delta \boldsymbol{\vartheta}_{N_h N_{\text{gal}}}) \sum_{i=1}^{N_h} \sum_{j=1}^{N_h} \sum_{k=1}^{N_h} u(|\boldsymbol{\theta}_1 - \boldsymbol{\vartheta}_i|)$$

$$\sum_{l=1}^{N_{\text{gal}}} \delta_{\text{D}}(\boldsymbol{\theta}_2 - \boldsymbol{\vartheta}_j - \Delta \boldsymbol{\vartheta}_{jl}) \sum_{m=1}^{N_{\text{gal}}} \delta_{\text{D}}(\boldsymbol{\theta}_3 - \boldsymbol{\vartheta}_k - \Delta \boldsymbol{\vartheta}_{km}) .$$

The delta ‘functions’ reduce the integrals, so the expression simplifies to

$$\langle N(\boldsymbol{\theta}_1) N(\boldsymbol{\theta}_2) \kappa(\boldsymbol{\theta}_3) \rangle$$

$$= A^{-N_h} K \int_A d^2 \boldsymbol{\vartheta}_1 \dots d^2 \boldsymbol{\vartheta}_{N_h} \quad (\text{A.9})$$

$$\sum_{i=1}^{N_h} \sum_{j=1}^{N_h} \sum_{k=1}^{N_h} \sum_{l=1}^{N_{\text{gal}}} \sum_{m=1}^{N_{\text{gal}}} u(|\boldsymbol{\theta}_1 - \boldsymbol{\vartheta}_i|) u(|\boldsymbol{\theta}_2 - \boldsymbol{\vartheta}_j|) u(|\boldsymbol{\theta}_3 - \boldsymbol{\vartheta}_k|)$$

$$= A^{-N_h} K N_{\text{gal}}^2 \int_A d^2 \boldsymbol{\vartheta}_1 \dots d^2 \boldsymbol{\vartheta}_{N_h} \quad (\text{A.10})$$

$$\sum_{i=1}^{N_h} \sum_{j=1}^{N_h} \sum_{k=1}^{N_h} u(|\boldsymbol{\theta}_1 - \boldsymbol{\vartheta}_i|) u(|\boldsymbol{\theta}_2 - \boldsymbol{\vartheta}_j|) u(|\boldsymbol{\theta}_3 - \boldsymbol{\vartheta}_k|)$$

We can split this triple sum into a 1-halo term with $i = j = k$, three 2-halo terms with $i = j \neq k$, $i = k \neq j$ and $j = k \neq i$ and a 3-halo term with $i \neq j \neq k$. Using $\int_A d^2 \boldsymbol{\vartheta} = A$ and $\int d^2 \boldsymbol{\vartheta} u(\boldsymbol{\vartheta}) = 1$, this leads to

$$\langle N(\boldsymbol{\theta}_1) N(\boldsymbol{\theta}_2) \kappa(\boldsymbol{\theta}_3) \rangle$$

$$= A^{-N_h} K N_{\text{gal}}^2 \sum_{i=1}^{N_h} A^{N_h-1} \quad (\text{A.11})$$

$$\int d^2 \boldsymbol{\vartheta} u(|\boldsymbol{\theta}_1 - \boldsymbol{\vartheta}|) u(|\boldsymbol{\theta}_2 - \boldsymbol{\vartheta}|) u(|\boldsymbol{\theta}_3 - \boldsymbol{\vartheta}|)$$

$$+ A^{-N_h} K N_{\text{gal}}^2 \sum_{i=1}^{N_h} \sum_{j \neq i}^{N_h} A^{N_h-2} \int d^2 \boldsymbol{\vartheta} u(|\boldsymbol{\theta}_1 - \boldsymbol{\vartheta}|) u(|\boldsymbol{\theta}_3 - \boldsymbol{\vartheta}|)$$

$$+ A^{-N_h} K N_{\text{gal}}^2 \sum_{i=1}^{N_h} \sum_{j \neq i}^{N_h} A^{N_h-2} \int d^2 \boldsymbol{\vartheta} u(|\boldsymbol{\theta}_1 - \boldsymbol{\vartheta}|) u(|\boldsymbol{\theta}_2 - \boldsymbol{\vartheta}|)$$

$$+ A^{-N_h} K N_{\text{gal}}^2 \sum_{i=1}^{N_h} \sum_{j \neq i}^{N_h} A^{N_h-2} \int d^2 \boldsymbol{\vartheta} u(|\boldsymbol{\theta}_2 - \boldsymbol{\vartheta}|) u(|\boldsymbol{\theta}_3 - \boldsymbol{\vartheta}|)$$

$$+ A^{-N_h} K N_{\text{gal}}^2 \sum_{i=1}^{N_h} \sum_{j \neq i}^{N_h} \sum_{k \neq i, k \neq j}^{N_h} A^{N_h-3}$$

$$= \frac{N_h K N_{\text{gal}}^2}{A} \int d^2 \boldsymbol{\vartheta} u(|\boldsymbol{\vartheta}_1 - \boldsymbol{\vartheta}|) u(|\boldsymbol{\vartheta}_2 - \boldsymbol{\vartheta}|) u(|\boldsymbol{\vartheta}_3 - \boldsymbol{\vartheta}|) \quad (\text{A.12})$$

$$+ \frac{N_h (N_h - 1) K N_{\text{gal}}^2}{A^2} \int d^2 \boldsymbol{\vartheta} u_i(|\boldsymbol{\vartheta}_1 - \boldsymbol{\vartheta}|) u_i(|\boldsymbol{\vartheta}_3 - \boldsymbol{\vartheta}|)$$

$$+ \frac{N_h (N_h - 1) K N_{\text{gal}}^2}{A^2} \int d^2 \boldsymbol{\vartheta} u(|\boldsymbol{\vartheta}_1 - \boldsymbol{\vartheta}|) u(|\boldsymbol{\vartheta}_2 - \boldsymbol{\vartheta}|)$$

$$+ \frac{N_h (N_h - 1) K N_{\text{gal}}^2}{A^2} \int d^2 \boldsymbol{\vartheta} u(|\boldsymbol{\vartheta}_2 - \boldsymbol{\vartheta}|) u(|\boldsymbol{\vartheta}_3 - \boldsymbol{\vartheta}|)$$

$$+ \frac{N_h (N_h - 1) (N_h - 2) K N_{\text{gal}}^2}{A^3} .$$

From this, we can infer $\langle N^2 M_{\text{ap}} \rangle$ with Eq. (12). Since the filter function U_θ is compensated, the integrals over constant terms

vanish and only the first term in the sum remains. Therefore, with the exponential filter function from Eq. (13) and $\bar{N} = N_h N_{\text{gal}}/A$ leads to Eq. (12),

$$\begin{aligned} & \langle \mathcal{N}^2 M_{\text{ap}} \rangle (\theta_1, \theta_2, \theta_3) \\ &= \frac{A K}{N_h (2\pi)^3} \int_0^\infty d^2 \vartheta \prod_{i=1}^3 \frac{1}{\theta_i^2} \end{aligned} \quad (\text{A.13})$$

$$\begin{aligned} & \int d^2 \vartheta_i u(|\vartheta_i - \vartheta|) \left(1 - \frac{\vartheta_i^2}{2\theta_i^2}\right) \exp\left(-\frac{\vartheta_i^2}{2\theta_i^2}\right) \\ &= \frac{A K}{N_h (2\pi)^2} \int_0^\infty d^2 \vartheta \prod_{i=1}^3 \frac{1}{\theta_i^2} \int_0^{2\pi} d\phi_i \int_0^\infty dy_i y_i u(y_i) \\ & \exp\left(-\frac{y_i^2 + \vartheta^2}{2\theta_i^2}\right) \left(1 - \frac{y_i^2 + \vartheta^2}{2\theta_i^2} - \frac{y_i \vartheta \cos(\phi_i)}{\theta_i^2}\right). \end{aligned} \quad (\text{A.14})$$

We can now use that

$$\int_0^{2\pi} dx \cos(x) \exp(-a \cos(x)) = -2\pi I_1(a), \quad (\text{A.15})$$

$$\int_0^{2\pi} dx \exp(-a \cos(x)) = 2\pi I_0(a), \quad (\text{A.16})$$

with the modified Bessel functions of the first kind I_n . We also introduce the scaled Bessel functions $f_n(x) = I_n(x) \exp(-x)$, so the aperture statistics are finally

$$\begin{aligned} & \langle \mathcal{N}^2 M_{\text{ap}} \rangle (\theta_1, \theta_2, \theta_3) \\ &= \frac{2\pi A K}{N_h} \int_0^\infty d\vartheta \vartheta \prod_{i=1}^3 \int_0^\infty dy_i \frac{y_i u(y_i)}{\theta_i^2} \exp\left[-\frac{(y_i - \vartheta)^2}{2\theta_i^2}\right] \\ & \left[\left(1 - \frac{y_i^2 + \vartheta^2}{2\theta_i^2}\right) f_0\left(\frac{y_i \vartheta}{\theta_i^2}\right) + \frac{y_i \vartheta}{\theta_i^2} f_1\left(\frac{y_i \vartheta}{\theta_i^2}\right) \right]. \end{aligned} \quad (\text{A.17})$$

Appendix B: Computational Implementation with Graphics Processing Units

Our estimates of $\tilde{\mathcal{G}}$ are computed by calculating the sums in Eqs. (4), (17) and (33) brute-force on a Graphics Processing Unit (GPU). Our algorithm (see Algorithm 1) for the estimation of $\tilde{\mathcal{G}}$ works similar to the procedures proposed by Bard et al. (2013) for the calculation of the galaxy two-point correlation and by Cárdenas-Montes et al. (2014) for the calculation of the galaxy two- and three-point function and the shear-shear correlation. It can be used both for two equal lens samples and two different lens samples.

This algorithm is implemented in CUDA 10 using double floating point precision. For the calculation we use an NVIDIA RTX 2080 Ti GPU, which has CUDA capability 7.5 and therefore enables 46×1024 parallel threads. Data is read from and written to ASCII files on an SSD hard drive, enabling fast data transfer.

Algorithm 1 Algorithm for the Computation of $\tilde{\mathcal{G}}$

```

Read in lens and source galaxy positions and source elliptici-
ties into main memory (RAM)
Copy galaxy positions and ellipticities from RAM to the GPU
Initialize container for  $\tilde{\mathcal{G}}$  with  $N_{\text{bins}}$  bins on RAM
Initialize container for  $\tilde{\mathcal{G}}$  with  $N_{\text{bins}}$  bins on GPU
Initialize  $N_{\text{th}}$  threads on GPU
In each thread  $i$  do
  for all sources  $j$  with  $j \in [i, i + N_{\text{th}}, i + 2N_{\text{th}}, \dots, N_s]$  do
    for all lenses do
      for all lenses do
        Get index of  $\tilde{\mathcal{G}}$  bin for this galaxy triplet
        Add contribution of this triplet to  $\tilde{\mathcal{G}}$  on GPU
      end for
    end for
  end for
end thread
Copy  $\tilde{\mathcal{G}}$  from GPU to RAM
Write  $\tilde{\mathcal{G}}$  to file

```
